

Simulation of two-phase flows at large density ratios and high Reynolds numbers using a discrete unified gas kinetic scheme

Jun Lai,^{1,2} Zuoli Xiao,¹ and Lian-Ping Wang^{2,3, a)}

¹⁾*State Key Laboratory for Turbulence and Complex Systems,
College of engineering, Peking University, Beijing 100871,
P.R. China*

²⁾*Guangdong Provincial Key Laboratory of Turbulence Research and Applications,
Center for Complex Flows and Soft Matter Research and Department of Mechanics
and Aerospace Engineering, Southern University of Science and Technology,
Shenzhen 518055, P.R. China*

³⁾*Guangdong-Hong Kong-Macao Joint Laboratory for Data-Driven Fluid Mechanics
and Engineering Applications, Southern University of Science and Technology,
Shenzhen 518055, China*

(Dated: 13 July 2022)

Abstract

In order to treat immiscible two-phase flows at large density ratios and high Reynolds numbers, a three-dimensional code based on the discrete unified gas kinetic scheme (DUGKS) is developed, incorporating two major improvements. First, the particle distribution functions at cell interfaces are reconstructed using a weighted essentially non-oscillatory scheme. Second, the conservative lower-order Allen-Cahn equation is chosen, instead of the higher-order Cahn-Hilliard equation, to evolve the free-energy-based phase field governing the dynamics of two-phase interfaces. Five benchmark problems are simulated to demonstrate the capability of the approach in treating two-phase flows at large density ratios and high Reynolds numbers, including three two-dimensional problems (a stationary droplet, Rayleigh-Taylor instability, and a droplet splashing on a thin liquid film) and two three-dimensional problems (binary droplets collision and Rayleigh-Taylor instability). All results agree well with the previous numerical and the experimental results. In these simulations, the density ratio and Reynolds number can reach a large value of $\mathcal{O}(1000)$. Our improved approach sets the stage for the DUGKS scheme to handle realistic two-phase flow problems.

^{a)}Electronic mail: wanglp@sustech.edu.cn

I. INTRODUCTION

Air-water two-phase flows are widespread phenomena in industry (hydroelectric power), agriculture (irrigation), medicine (intravenous injection), nature (rain) and our daily life (shower). The density ratio between water and air is about 800. A deep understanding of this kind of multiphase flows with large-density-ratio can promote the development of science and technology.

There are three approaches to study multiphase flows, including theoretical analysis, experiment observations and numerical simulations. Theoretical analysis can only deal with the simplest problems. Experiments rely on instruments, and may have a limited ability to capture the space-time evolution at the air-water interface scale, and are affected by the environmental conditions. In recent years, numerical simulation has developed rapidly and becomes an important approach for multiphase flow research. One of the common challenges with numerical methods is the numerical instability at large-density-ratios, and reliable numerical methods at large-density-ratio remain much desired. Much attention has been paid to dealing with the multiphase flow simulations at large-density-ratios in recent years.¹⁻⁹

In so-called interface-resolved multiphase flow simulations, the tracking of two-phase interfaces is essential. The traditional approaches based on Navier-Stokes solvers include the front-tracking method,¹⁰ volume-of-fluid (VOF) method,^{11,12} level-set (LS) method,^{12,13} *etc.* It remains challenging for the front-tracking method to model interface breakup and coalescence, because the interface needs to be artificially ruptured.^{10,14} For the VOF and LS methods, an interface reconstruction step is required, which would be a complex task to implement.^{11,14} Furthermore, the VOF method relies on the refinement of the grid when dealing with the flow interface, the mass conservation is well observed, but the accuracy in dealing with complex sharp interfaces is limited. The LS method has a superior capability in treating complex interfaces, and its tracking accuracy of free surface is typically higher than the VOF method. However, frequent reinitializations of the LS function are needed, which may cause errors in mass conservation.

The physical width of the fluid-fluid interface is much smaller than the macroscopic scale. It is beneficial to deal with the interface from a multiscale perspective. The mesoscopic simulation approaches for fluid-fluid two-phase flows have been developed based on the model Boltzmann equations over the past three decades. The two-phase mesoscopic models contain color-gradient model,¹⁵ pseudo-potential model,^{16,17} free-energy model,¹⁸ *etc.* Gunstensen *et al.*¹⁵ proposed the color-gradient model, which is based on the cellular automata model presented by Rothmann and

Keller.¹⁹ The surface tension is generated by a perturbation operator, causing some unphysical velocity near the interface.^{14,20,21} Shan and Chen¹⁶ developed the pseudo-potential model (Shan-Chen model), which features simple formulation and high computational efficiency. Furthermore, Shan-Chen model can separate fluid phases or components naturally, due to microscopic particle interactions.^{20,22} However, the surface tension is related to the density ratio, and spurious currents are non-negligible around the interface.^{14,23} Later, Swift *et al.*¹⁸ proposed the free-energy model. The free-energy-based phase-field model is thermodynamically more consistent than the above models,^{14,20} and is expected to be physically more capable.

As noted before, large-density-ratio multiphase flows are not easy to simulate. If Reynolds number is also considered, maintaining numerical stability becomes more challenging. Coupled Shan-Chen model with multiple-relaxation-time (MRT) collision operator, Li *et al.*²² simulated two-phase flows (droplet splashing on a thin film) with density ratio and Reynolds number up to $\rho^* \sim 700, Re \sim 1000$. The lattice velocity model is D2Q9, hence they only performed two-dimensional (2D) simulations. The main contribution to improved numerical stability is the MRT collision operator, which is a common and effective tool to calculate large-density-ratio multiphase flows in the mesoscopic approaches. They pointed out that the MRT collision operators are generally more stable than the standard Bhatnagar-Gross-Krook (BGK) collision operator.²⁴ We note that there are two possible reasons. From a mathematical point of view, the MRT model has more tunable parameters and more degrees of freedom. From a physical point of view, the relaxation time corresponding to different physical quantities may be different, and the MRT model can be more consistent with the physical principle. The MRT model was also incorporated into the color-gradient method for the large-density-ratio simulations, which was studied by Ba *et al.*²¹ with the D2Q9 lattice velocity model. Their results showed that $\rho^* \sim 1000$ for the steady flows (a static droplet and the layered channel flow), and $\rho^* \sim 100, Re \sim 500$ can be reached for the unsteady flow (a droplet splashing on a thin film).

In the phase-field model, the Allen-Cahn (AC) equation²⁵⁻²⁷ and Cahn-Hilliard (CH)^{28,29} equation are the two common models for the evolution of the phase field ϕ . It is noted that the CH equation is a fourth-order partial differential equation (PDE), while the AC equation is a second-order PDE which is easier to implement numerically and tends to be more stable. Wang *et al.*³⁰ compared AC equation and CH equation in the framework of LB models, and demonstrated that AC equation has a better numerical stability. Hence the AC equation is more suitable for the large-density-ratio two-phase-flow simulations⁴⁻⁹.

The CH equation can also treat large-density-ratio flows under some specific formulations. Wang *et al.*^{1,2} proposed multiphase lattice Boltzmann flux solvers (MLBFS) to simulate flows with $\rho^* \sim 1000$, and the Reynolds number could be greater than 1000. In MLBFS, the hydrodynamic equations are the combination of Navier-Stokes equations (NSE) and lattice Boltzmann equations (LBE). The LBE is utilized for the computation of the flux terms in NSE, while the NSE is discretized by the finite volume scheme. The Poisson equation for pressure does not need to be solved, hence this method combines the advantages of traditional and mesoscopic algorithms. Furthermore, a finite difference scheme is used for the CH equation, in which the convective term is solved by the weighted essentially non-oscillatory (WENO) scheme. We note that the WENO scheme³¹ is based on the essentially non-oscillatory (ENO) scheme.³² In ENO scheme, the smoothest stencil is selected to approximate the flux at cell boundary, which can reduce the numerical oscillations. In WENO scheme, the convex combination of all stencils is used and the weights of the stencils are properly chosen to improve the local accuracy. It is expected that the WENO scheme can also reduce the oscillation and enhance the numerical stability in the multiphase flow simulations. Chen *et al.*³ proposed a simplified multiphase lattice Boltzmann method (SMLBM) for the 2D (D2Q9) large-density-ratio ($\rho^* \sim 1000$) simulations. In SMLBM, they directly updated the macroscopic variables resolved in a predictor-corrector scheme, instead of the mesoscopic distribution functions.

A few studies coupled the LB method with the more stable phase-field equation (AC equation) to simulate the large-density-ratio problems. We denote this method as PF(AC)-LBM. Liang *et al.*^{4,5} simulated large-density-ratio multiphase flows by PF(AC)-LBM with BGK collision operator. The parameters can reach $\rho^* \sim 1000, Re \sim 500$ for the case of a 2D droplet splashing on a thin liquid film,⁴ and $\rho^* > 800, Re \sim 500$ for the case of a 3D droplet impact on a wetting solid.⁵ Furthermore, the numerical stability performance can be improved when combined with other techniques. Incorporating the MRT collision operator, Fakhari *et al.*⁶ used PF(AC)-LBM to perform the 2D Rayleigh-Taylor instability simulations with density ratio and Reynolds number up to $\rho^* \sim 1000, Re \sim 3000$. Based on the open-source LB framework,³³ Kumar *et al.*⁷ simulated 2D Rayleigh-Taylor instability with $\rho^* \sim 1000, Re \sim 3000$ when combining PF(AC)-LBM with the MRT collision operator.

As a relatively new mesoscopic approach, the discrete unified gas kinetic scheme (DUGKS)^{34,35} combines the advantages of the LBM^{20,36} and unified gas kinetic scheme (UGKS).³⁷ In DUGKS, the model Boltzmann equation is solved using an accurate finite-volume formulation coupling

tightly the kinetic particle transport and particle collisions. Compared to LBM, DUGKS can more easily incorporate irregular meshes and different kinetic particle velocity models. Hence we wish to explore the capability for DUGKS to simulate large-density-ratio multiphase flows. Based on the PF(AC)-DUGKS method, Yang *et al.*⁸ could simulate 2D Rayleigh-Taylor instability with large-density-ratio ($\rho^* \sim 1000$) but the Reynolds number is small ($Re \sim 50$). Combined with the adaptive mesh refinement technique, a multilevel PF(AC)-DUGKS was proposed by Yang *et al.*⁹ to simulate a 2D droplet splashing on a thin film with $\rho^* \sim 1000$, $Re \sim 500$.

To summarize, there are several ways to help improve the numerical stability and increase the density ratio in the multiphase flow simulations:

1. Incorporating the WENO scheme when treating the convective term;^{1,2}
2. Combining the macroscopic equations / variables and mesoscopic approaches;¹⁻³
3. Adopting the MRT collision operator instead of the BGK collision operator;^{6,7,21,22}
4. Using the AC equation instead of the CH equation in the phase-field approach.⁴⁻⁹

In the present work, we aim to extend the DUGKS scheme to simulate 3D multiphase flows at large density ratios and higher Reynolds numbers. For this purpose, we couple Yang *et al.*⁸'s PF(AC)-DUGKS algorithm with the WENO scheme at the cell interface to improve the numerical stability. The D3Q19 lattice velocity model is used, with a parallel implementation strategy to address the computing resources requirement.

The rest of the paper is organized as follows. In Section II, the governing equations and the numerical methods for the large-density-ratio two-phase flows are presented. In Section III and IV, 2D benchmark problems (a stationary droplet, Rayleigh-Taylor instability, and a droplet splashing on a thin liquid film) and 3D benchmark problems (binary droplets collision and Rayleigh-Taylor instability) are validated and analyzed. Finally, conclusions are given in Section V.

II. METHODOLOGY

A. The phase-field theory and governing equations for two-phase flows

In the phase-field theory, the free energy functional of fluid-fluid two-phase flow contains the bulk free-energy and the interfacial free-energy, and can be expressed as³⁸⁻⁴⁴

$$\mathcal{F}(\phi, \nabla\phi) = \int_V \left[\psi(\phi) + \frac{\kappa}{2} |\nabla\phi|^2 \right] dV, \quad (1)$$

where ϕ is the order parameter corresponding to the two phases. $\psi(\phi) = \beta(\phi - \phi_A)^2(\phi - \phi_B)^2$ is the free-energy density of the bulk fluids, representing separation of the two phases into the bulk region. $\frac{\kappa}{2} |\nabla\phi|^2$ is the free-energy density of the interfacial region, representing mixing of the two phases. V is the volume of the considered domain. $\phi_A = 1$ and $\phi_B = 0$ are parameters corresponding to the two phases. β and κ are positive coefficients that determine the relative magnitudes of bulk free-energy density and interfacial free-energy density, respectively. They also relate to the surface tension σ and the interfacial thickness parameter W , *i.e.*,

$$\sigma = \frac{|\phi_A - \phi_B|^3}{6} \sqrt{2\kappa\beta}, \quad W = \frac{1}{\phi_A - \phi_B} \sqrt{\frac{8\kappa}{\beta}}. \quad (2)$$

The chemical potential μ_ϕ is the variation of the free energy functional $\mathcal{F}(\phi, \nabla\phi)$ with respect to ϕ ,^{42,43}

$$\mu_\phi = \frac{\delta\mathcal{F}}{\delta\phi} = 4\beta(\phi - \phi_A)(\phi - \phi_B) \left(\phi - \frac{\phi_A + \phi_B}{2} \right) - \kappa\nabla^2\phi. \quad (3)$$

For a flat interface at equilibrium, $\mu_\phi^{eq} = 0$. Then ϕ can be obtained as^{40,43}

$$\phi^{eq}(\zeta) = \frac{\phi_A + \phi_B}{2} + \frac{\phi_A - \phi_B}{2} \tanh\left(\frac{2\zeta}{W}\right), \quad (4)$$

where ζ is the signed distance normal to the interface.

Next, we discuss the time evolution of the order parameter ϕ . The governing equation of ϕ can be written in terms of the flux densities as a conservative form⁴⁵

$$\frac{\partial\phi}{\partial t} = -\nabla \cdot (\mathbf{j}_A + \mathbf{j}_D + \mathbf{j}_S), \quad (5)$$

where t is the time. \mathbf{j}_A , \mathbf{j}_D and \mathbf{j}_S are the advective flux density, the diffusive flux density, and the phase separation flux density. The advective flux is $\mathbf{j}_A = \phi\mathbf{u}$, where \mathbf{u} is the flow velocity.

The AC equation is utilized here to help treat large density ratios. For the conservative AC equation, the diffusive flux is expressed as⁴⁵

$$\mathbf{j}_D = -M_{AC}\nabla\phi, \quad (6)$$

where M_{AC} is the mobility.

The phase separation flux density can be determined by the equilibrium profile of ϕ , Eq. (4). Considering a flat interface located on $x = 0$ at the equilibrium state, Eq. (5) should be satisfied. In this case, $\partial_t \phi^{eq} = 0$ and $\mathbf{j}_A^{eq} = \mathbf{0}$, leading to $\nabla \cdot (\mathbf{j}_D^{eq} + \mathbf{j}_S^{eq}) = 0$. A simple choice is

$$\mathbf{j}_S^{eq} = -\mathbf{j}_D^{eq}, \quad (7)$$

where

$$\begin{aligned} \mathbf{j}_D^{eq} &= -M_{AC} \mathbf{e}_x \frac{d}{dx} \phi^{eq}(x) \\ &= -M_{AC} \mathbf{e}_x \frac{\phi_A - \phi_B}{W} \left[1 - \tanh^2 \left(\frac{2x}{W} \right) \right] \\ &= -M_{AC} \mathbf{e}_x \frac{4[\phi_A - \phi^{eq}(x)][\phi^{eq}(x) - \phi_B]}{W(\phi_A - \phi_B)}. \end{aligned} \quad (8)$$

Therefore, for a curved interface, the phase separation flux density can be designed as

$$\mathbf{j}_S = M_{AC} \frac{4(\phi_A - \phi)(\phi - \phi_B)}{W(\phi_A - \phi_B)} \frac{\nabla \phi}{|\nabla \phi|}. \quad (9)$$

Combining with the mass equation and the momentum equation, then the macroscopic governing equations (ACNS system) of immiscible two-phase flows are⁸

$$\frac{\partial \phi}{\partial t} + \nabla \cdot (\phi \mathbf{u}) = \nabla \cdot [M_{AC} (\nabla \phi - \theta \mathbf{n})], \quad (10a)$$

$$\nabla \cdot \mathbf{u} = 0, \quad (10b)$$

$$\frac{\partial (\rho \mathbf{u})}{\partial t} + \nabla \cdot (\rho \mathbf{u} \mathbf{u}) = -\nabla p + \nabla \cdot [\mu (\nabla \mathbf{u} + \mathbf{u} \nabla)] + \mathbf{F}, \quad (10c)$$

where $\theta = \frac{-4(\phi - \phi_A)(\phi - \phi_B)}{W(\phi_A - \phi_B)}$ is a parameter related to ϕ , $\mathbf{n} = \frac{\nabla \phi}{|\nabla \phi|}$ is the normal unit vector of the ϕ field. p is the pressure. $\mathbf{F} = \mathbf{F}_s + \mathbf{F}_b$ is the total body force, where $\mathbf{F}_s = \mu_\phi \nabla \phi$ is the interfacial force and \mathbf{F}_b contains other body forces such as gravity. It is noted that $\mathbf{F}_s = \mu_\phi \nabla \phi$ instead of the alternative form $\mathbf{F}_s = -\phi \nabla \mu_\phi$ to reduce the order of spatial derivatives in the simulations. The fluid density ρ and dynamic viscosity μ are given by the linear models⁴⁶ as

$$\rho = \frac{\phi - \phi_B}{\phi_A - \phi_B} \rho_A + \frac{\phi - \phi_A}{\phi_B - \phi_A} \rho_B, \quad (11a)$$

$$\mu = \frac{\phi - \phi_B}{\phi_A - \phi_B} \mu_A + \frac{\phi - \phi_A}{\phi_B - \phi_A} \mu_B, \quad (11b)$$

where ρ_A , ρ_B and μ_A , μ_B are the densities and the dynamic viscosities of the two phases.

It is noted that the density ρ is determined by the order parameter ϕ , and is independent of the pressure p . Substituting Eq. (11a) and Eq. (10b) into Eq. (10a), leading to the equation of density as

$$\frac{\partial \rho}{\partial t} + \nabla \cdot (\rho \mathbf{u}) = \frac{\rho_A - \rho_B}{\phi_A - \phi_B} \nabla \cdot [M_{AC}(\nabla \phi - \theta \mathbf{n})]. \quad (12)$$

Therefore, the mass is not locally conserved in this model. In the single-phase region, $\nabla \phi = \mathbf{0}$ and $\theta = 0$, then the right hand side (RHS) of Eq. (12) is zero. If the densities of the two phases are the same, then $\rho_A = \rho_B$ and the RHS of Eq. (12) is also zero. As a result, the nonconservative mass problem only happens near the two-phase interface when the densities of the two fluids are different. The mass conservation could be restored by a quasi-incompressible model,^{42,43,47} where the velocity-divergence is modified. Hence in the quasi-incompressible model, the flow field is not incompressible precisely near the two-phase interface if the density-ratio is not one.

B. The mesoscopic model for the ACNS system

The double-distribution function model is used to reproduce the conservative AC equation and the hydrodynamic equations. The following two model Boltzmann equations with a Bhatnager-Gross-Krook (BGK) collision model⁴⁸ are employed⁸

$$\frac{\partial f_\alpha}{\partial t} + \xi_\alpha \cdot \nabla f_\alpha = -\frac{f_\alpha - f_\alpha^{eq}}{\tau_f} + S_\alpha^f, \quad (13a)$$

$$\frac{\partial g_\alpha}{\partial t} + \xi_\alpha \cdot \nabla g_\alpha = -\frac{g_\alpha - g_\alpha^{eq}}{\tau_g} + S_\alpha^g, \quad (13b)$$

where the distribution functions $f_\alpha = f_\alpha(\mathbf{x}, t)$ and $g_\alpha = g_\alpha(\mathbf{x}, t)$ corresponding to a discrete particle velocity ξ_α are functions of position \mathbf{x} and time t . τ_f and τ_g are the relaxation times. The key to recover the macroscopic governing equations is to properly design the two equilibrium distribution functions (f_α^{eq} , g_α^{eq}) and the two source terms (S_α^f , S_α^g).

Applying the Chapman-Enskog analysis,⁴⁹ we can derive the moment-integral constraints for the equilibrium distribution functions and the source terms, to recover the ACNS system, as shown in Appendix A. There are many possible designs, and one specific design is presented here. For the phase-field, we adopt the following design^{4,8,9,30}

$$f_\alpha^{eq} = \omega_\alpha \phi \left(1 + \frac{\xi_\alpha \cdot \mathbf{u}}{RT} \right), \quad (14a)$$

$$S_\alpha^f = \omega_\alpha \xi_\alpha \cdot \theta \mathbf{n} + \frac{\omega_\alpha \xi_\alpha}{RT} \cdot \frac{\partial (\phi \mathbf{u})}{\partial t}. \quad (14b)$$

The equilibrium distribution function and the source terms for the hydrodynamic variables can be specified as^{4,8,44,50}

$$g_\alpha^{eq} = \begin{cases} s_0 \rho + (\omega_0 - 1) \frac{p}{RT}, & \alpha = 0, \\ s_\alpha \rho + \omega_\alpha \frac{p}{RT}, & \alpha \neq 0, \end{cases} \quad (15a)$$

$$S_\alpha^g = \frac{\xi_\alpha \cdot \mathbf{u}}{RT} \cdot [(\omega_\alpha + s_\alpha) \mathbf{F} + s_\alpha RT \nabla \rho], \quad (15b)$$

where

$$s_\alpha = \omega_\alpha \left[\frac{\xi_\alpha \cdot \mathbf{u}}{RT} + \frac{(\xi_\alpha \cdot \mathbf{u})^2}{2(RT)^2} - \frac{u^2}{2RT} \right]. \quad (16)$$

For the discrete-velocity model, the D3Q19 model (the number of the discrete velocities $Q = 19$) is used, with

$$\xi_\alpha = \begin{cases} (0, 0, 0)c, & \alpha = 0, \\ (\pm 1, 0, 0)c, (0, \pm 1, 0)c, (0, 0, \pm 1)c, & \alpha = 1 - 6, \\ (0, \pm 1, \pm 1)c, (\pm 1, 0, \pm 1)c, (\pm 1, \pm 1, 0)c, & \alpha = 7 - 18, \end{cases} \quad (17)$$

where $c = \sqrt{3RT} = 1$ in lattice unit, R is the model gas constant, T is the reference temperature. The weighting coefficients are $\omega_0 = 1/3$, $\omega_{1-6} = 1/18$, $\omega_{7-18} = 1/36$, respectively.

C. Discrete unified gas kinetic scheme (DUGKS)

The DUGKS approach^{34,35} is a finite-volume scheme to solve the model Boltzmann equation. For the sake of discussion, Eqs. (13) are written into the following unified form^{8,42}

$$\frac{\partial \varphi_\alpha}{\partial t} + \xi_\alpha \cdot \nabla \varphi_\alpha = \Omega_\alpha^\varphi + S_\alpha^\varphi, \quad (18)$$

where φ denotes the distribution function f or g , and $\Omega_\alpha^\varphi = -(\varphi_\alpha - \varphi_\alpha^{eq})/\tau_\varphi$ is the corresponding collision term.

First, we integrate Eq. (18) in space (control volume V_j) and time (from t_n to t_{n+1}), obtaining

$$\begin{aligned} & \varphi_\alpha^{n+1} - \varphi_\alpha^n + \frac{\Delta t}{|V_j|} J_\alpha^{n+1/2} \\ &= \frac{\Delta t}{2} \left(\Omega_\alpha^{\varphi, n+1} + \Omega_\alpha^{\varphi, n} \right) + \frac{\Delta t}{2} \left(S_\alpha^{\varphi, n+1} + S_\alpha^{\varphi, n} \right), \end{aligned} \quad (19)$$

where the volume average of the distribution function at t_n is

$$\varphi_\alpha^n = \frac{1}{|V_j|} \int_{V_j} \varphi_\alpha(\mathbf{x}, t_n) dV, \quad (20a)$$

the flux across the cell interface at $t_{n+1/2}$ is

$$J_\alpha^{n+1/2} = \int_{A_j} (\boldsymbol{\xi}_\alpha \cdot \mathbf{n}) \varphi_\alpha(\mathbf{x}, t_{n+1/2}) dA, \quad (20b)$$

the volume average of the collision term and the source term at t_n are, respectively,

$$\Omega_\alpha^{\varphi,n} = \frac{1}{|V_j|} \int_{V_j} \Omega_\alpha^\varphi(\mathbf{x}_j, t_n) dV, \quad (20c)$$

$$S_\alpha^{\varphi,n} = \frac{1}{|V_j|} \int_{V_j} S_\alpha^\varphi(\mathbf{x}_j, t_n) dV. \quad (20d)$$

$\Delta t = t_{n+1} - t_n$. $|V_j|$ and A_j are the volume and surface of V_j , respectively. It is noted that the midpoint rule is utilized for the advection term and trapezoidal rule for the collision term and the source term in Eq. (19).

Separating the terms at the same time step, Eq. (19) can be written in an explicit form as

$$\tilde{\varphi}_\alpha^{n+1} = \tilde{\varphi}_\alpha^{+,n} - \frac{\Delta t}{|V_j|} J_\alpha^{n+1/2}, \quad (21)$$

in which the auxiliary distribution functions are

$$\begin{aligned} \tilde{\varphi}_\alpha &= \varphi_\alpha - \frac{\Delta t}{2} (\Omega_\alpha^\varphi + S_\alpha^\varphi) \\ &= \frac{2\tau_\varphi + \Delta t}{2\tau_\varphi} \varphi_\alpha - \frac{\Delta t}{2\tau_\varphi} \varphi_\alpha^{eq} - \frac{\Delta t}{2} S_\alpha^\varphi, \end{aligned} \quad (22a)$$

$$\begin{aligned} \tilde{\varphi}_\alpha^+ &= \varphi_\alpha + \frac{\Delta t}{2} (\Omega_\alpha^\varphi + S_\alpha^\varphi) \\ &= \frac{2\tau_\varphi - \Delta t}{2\tau_\varphi + \Delta t} \tilde{\varphi}_\alpha + \frac{2\Delta t}{2\tau_\varphi + \Delta t} \varphi_\alpha^{eq} + \frac{2\tau_\varphi \Delta t}{2\tau_\varphi + \Delta t} S_\alpha^\varphi. \end{aligned} \quad (22b)$$

To update $\tilde{\varphi}_\alpha^{n+1}$, the key is to evaluate the flux across the cell interface at half time step $t_{n+1/2}$. Integrating Eq. (18) from t_n to $t_{n+1/2}$ along the characteristic line, yields

$$\begin{aligned} &\varphi_\alpha(\mathbf{x}_{j+1/2}, t_n + h) - \varphi_\alpha(\mathbf{x}_{j+1/2} - \boldsymbol{\xi}_\alpha h, t_n) \\ &= \frac{h}{2} [\Omega_\alpha^\varphi(\mathbf{x}_{j+1/2}, t_n + h) + \Omega_\alpha^\varphi(\mathbf{x}_{j+1/2} - \boldsymbol{\xi}_\alpha h, t_n)] \\ &\quad + \frac{h}{2} [S_\alpha^\varphi(\mathbf{x}_{j+1/2}, t_n + h) + S_\alpha^\varphi(\mathbf{x}_{j+1/2} - \boldsymbol{\xi}_\alpha h, t_n)], \end{aligned} \quad (23)$$

where $h = \Delta t/2$ denotes the half time step size, the interface location $\mathbf{x}_{j+1/2} = (\mathbf{x}_j + \mathbf{x}_{j+1})/2$ for the uniform grid.

Similarly, Eq. (23) can be reduced in an explicit form as

$$\bar{\varphi}_\alpha(\mathbf{x}_{j+1/2}, t_n + h) = \bar{\varphi}_\alpha^+(\mathbf{x}_{j+1/2} - \boldsymbol{\xi}_\alpha h, t_n), \quad (24)$$

where another two auxiliary distribution functions are introduced as

$$\bar{\varphi}_\alpha = \frac{2\tau_\varphi + h}{2\tau_\varphi} \varphi_\alpha - \frac{h}{2\tau_\varphi} \varphi_\alpha^{eq} - \frac{h}{2} S_\alpha^\varphi, \quad (25a)$$

$$\bar{\varphi}_\alpha^+ = \frac{2\tau_\varphi - h}{2\tau_\varphi + h} \bar{\varphi}_\alpha + \frac{2h}{2\tau_\varphi + h} \varphi_\alpha^{eq} + \frac{2\tau_\varphi h}{2\tau_\varphi + h} S_\alpha^\varphi. \quad (25b)$$

The RHS of Eq. (24) is evaluated using the first-order Taylor expansion,

$$\bar{\varphi}_\alpha^+(\mathbf{x}_{j+1/2} - \boldsymbol{\xi}h, t_n) \approx \bar{\varphi}_\alpha^+(\mathbf{x}_{j+1/2}, t_n) - \boldsymbol{\xi}_\alpha h \cdot \boldsymbol{\sigma}_{j+1/2}, \quad (26)$$

where $\boldsymbol{\sigma}_{j+1/2} = \nabla \bar{\varphi}_\alpha^+(\mathbf{x}_{j+1/2}, t_n)$. To enhance the numerical stability of the PF(AC)-DUGKS approach, the distribution function $\bar{\varphi}_\alpha^+(\mathbf{x}_{j+1/2}, t_n)$ is reconstructed using the WENO scheme, which is discussed in Section II D.

The original distribution function at the half time step $\varphi_\alpha(\mathbf{x}_{j+1/2}, t_n + h)$ can be obtained by Eq. (25a) as

$$\varphi_\alpha = \frac{2\tau_\varphi}{2\tau_\varphi + h} \bar{\varphi}_\alpha + \frac{h}{2\tau_\varphi + h} \varphi_\alpha^{eq} + \frac{\tau_\varphi h}{2\tau_\varphi + h} S_\alpha^\varphi. \quad (27)$$

It is used to evaluate $\mathbf{J}_\alpha^{n+1/2}$ in Eq. (20b).

Furthermore, we can show the following relationship of the auxiliary distribution functions,

$$\tilde{\varphi}_\alpha^+ = \frac{4}{3} \bar{\varphi}_\alpha^+ - \frac{1}{3} \tilde{\varphi}_\alpha, \quad (28a)$$

$$\bar{\varphi}_\alpha^+ = \frac{2\tau_\varphi - h}{2\tau_\varphi + \delta t} \tilde{\varphi}_\alpha + \frac{3h}{2\tau_\varphi + \delta t} \varphi_\alpha^{eq} + \frac{3\tau_\varphi h}{2\tau_\varphi + \delta t} S_\alpha^\varphi. \quad (28b)$$

In the end, from Eq. (21) we can obtain $\tilde{\varphi}_\alpha$, which is the distribution function tracked in the DUGKS approach.

For the ACNS system, the macroscopic variables are evaluated as^{4,8}

$$\phi(\mathbf{x}_j, t_n + \Delta t) = \sum_{\alpha=0}^{Q-1} \tilde{f}_\alpha, \quad (29a)$$

$$\mathbf{u}(\mathbf{x}_j, t_n + \Delta t) = \frac{1}{\rho} \left(\sum_{\alpha=0}^{Q-1} \boldsymbol{\xi}_\alpha \tilde{g}_\alpha + \frac{\Delta t}{2} \mathbf{F} \right), \quad (29b)$$

$$p(\mathbf{x}_j, t_n + \Delta t) = \frac{RT}{1 - \omega_0} \left(\sum_{\alpha=1}^{Q-1} \tilde{g}_\alpha + \frac{\Delta t}{2} \mathbf{u} \cdot \nabla \rho + \rho s_0 \right). \quad (29c)$$

The time step size is related to the Courant-Friedrichs-Lewy (CFL) condition^{34,37,42,51}

$$\Delta t = CFL \frac{\Delta x_{\min}}{\sqrt{3RT}}, \quad (30)$$

where Δx_{\min} is the minimal grid spacing, CFL is the CFL number.

It should be noted that the two source terms and the computation of macroscopic variables involve first-order and second-order spatial derivatives, they are evaluated by second-order spatial central finite difference schemes. The first-order time derivative in the computation the macroscopic variables is approximated by a backward Euler scheme.

D. The WENO treatment for the distribution functions at the cell interface

The key idea in the WENO scheme is that a combination of all neighbor stencils is used to approximate the flux at the cell boundary, and the weights of the stencils are chosen appropriately. The smoother stencil has a larger weight. Hence it is expected to reduce the numerical oscillation and improve the stability of the multiphase flow simulations.^{1,2,31} Chen *et al.*⁵¹ has coupled WENO with DUGKS scheme to improve the spatial accuracy and the numerical stability, which can capture shocklet in single-phase compressible decaying isotropic turbulence. Their results showed that the incorporation of WENO allows DUGKS to obtain better numerical results.

Here the 3rd-order classical WENO scheme^{31,51} is employed to improve the numerical stability of the PF(AC)-DUGKS two-phase scheme. We take a cell interface located at $x_{j+1/2}$ and normal to x -direction at time t_n as an example. If the x component of the discrete particle velocity is positive ($\xi_{\alpha x} > 0$) at the position $x_{j+1/2}$, then the approximate cell interface results based on different stencils are

$$\bar{\varphi}_{\alpha}^{+(0)}(x_{j+1/2}, t_n) = -\frac{1}{2}\bar{\varphi}_{\alpha}^{+}(x_{j-1}, t_n) + \frac{3}{2}\bar{\varphi}_{\alpha}^{+}(x_j, t_n), \quad (31a)$$

$$\bar{\varphi}_{\alpha}^{+(1)}(x_{j+1/2}, t_n) = \frac{1}{2}\bar{\varphi}_{\alpha}^{+}(x_j, t_n) + \frac{1}{2}\bar{\varphi}_{\alpha}^{+}(x_{j+1}, t_n). \quad (31b)$$

The indicators of the smoothness are first defined by Liu *et al.*,⁵² which can be expressed as

$$\beta_0 = [\bar{\varphi}_{\alpha}^{+}(x_{j-1}, t_n) - \bar{\varphi}_{\alpha}^{+}(x_j, t_n)]^2, \quad (32a)$$

$$\beta_1 = [\bar{\varphi}_{\alpha}^{+}(x_j, t_n) - \bar{\varphi}_{\alpha}^{+}(x_{j+1}, t_n)]^2. \quad (32b)$$

It is noted that β_0, β_1 would be larger/smaller when $\bar{\varphi}_{\alpha}^{+}$ is discontinuous/continuous on the stencils considered. Hence they represent the smoothness of $\bar{\varphi}_{\alpha}^{+}$.⁵² Then the nonlinear weights are

$$\omega_0 = \frac{\tilde{\omega}_0}{\tilde{\omega}_0 + \tilde{\omega}_1}, \quad \omega_1 = \frac{\tilde{\omega}_1}{\tilde{\omega}_0 + \tilde{\omega}_1}, \quad (33)$$

with

$$\tilde{\omega}_0 = \frac{\gamma_0}{(\varepsilon + \beta_0)^2}, \quad \tilde{\omega}_1 = \frac{\gamma_1}{(\varepsilon + \beta_1)^2}, \quad (34)$$

where $\gamma_0 = 1/3$, $\gamma_1 = 2/3$ are the linear weights. A small constant $\varepsilon = 10^{-6}$ is needed in order to make the denominator non-zero.^{31,51,52}

In the end, the distribution function at the cell interface $x_{j+1/2}$ can be reconstruction as the following convex combination

$$\bar{\varphi}_\alpha^+(x_{j+1/2}, t_n) = \omega_0 \bar{\varphi}_\alpha^{+(0)}(x_{j+1/2}, t_n) + \omega_1 \bar{\varphi}_\alpha^{+(1)}(x_{j+1/2}, t_n). \quad (35)$$

For $\xi_{\alpha x} < 0$, the results are similar based on the upwind scheme. For $\xi_{\alpha x} = 0$, an average of the results from $\xi_{\alpha x} > 0$ and $\xi_{\alpha x} < 0$ is taken. For the cell interfaces in the y direction and z direction, the procedures are the same as those in the x direction.

III. TWO DIMENSIONAL SIMULATIONS AND DISCUSSIONS

First, we utilize the 3D code to model 2D problems in this section, to demonstrate that this code can simulate dimensionality reduction problems very well. The computational domain is $[0, N_x] \times [0, N_y] \times [0, 2]$ in the 2D simulations. Since the variables of the two grid nodes in z direction are the same, we only mention $[0, N_x] \times [0, N_y]$ or $[-N_x/2, N_x/2] \times [-N_y/2, N_y/2]$ for simplicity.

A. A stationary droplet and the Young-Laplace law

A stationary liquid droplet is first simulated to validate our PF(AC)-DUGKS-WENO code. All the parameters are in lattice units in this paper. Initially, a circular droplet is placed at the center of the computational domain of size $[-L, L] \times [-L, L] = 128^2$. The periodic boundary conditions are applied in all spatial directions. To model the two phases similar as water and air, the density ratio is $\rho^* = \rho_A/\rho_B = 1000$ and kinematic viscosity ratio is $\nu^* = \nu_A/\nu_B = 0.06$, these same ratios were used by Lycett-Brown and Luo.⁵³ $M_{AC} = 1.0 \times 10^{-6}$ is chosen and $W = 5.0$. There is no gravity in this simulation. The CFL number is $CFL = 0.25$. The order parameter is initialized as^{23,42,43,50}

$$\phi(r_2) = \frac{\phi_A + \phi_B}{2} + \frac{\phi_A - \phi_B}{2} \tanh\left(2 \frac{R_0 - r_2}{W}\right), \quad (36)$$

where $r_2 = \sqrt{(x - x_c)^2 + (y - y_c)^2}$ is the distance between any point (x, y) in the computational domain and the droplet center (x_c, y_c) . The initial velocity is zero in the whole domain. The

pressure is initialized as $p = \phi \sigma / R_0$, in order for the simulation to reach the steady state faster. In this case, the dimensionless time is defined as $t^* = \frac{t}{R_0} \sqrt{\frac{\sigma}{\rho R_0}}$. For testing the Young-Laplace law and comparing with the previous studies,^{8,42} 18 cases are simulated. The radii of the droplets are selected as $R_0 = 20, 24, 28, 32, 36, 40$, and the surface tensions are $\sigma = 0.001, 0.005, 0.01$.

The convergence criterion for the static flows in Yang *et al.*⁸ is

$$\delta\Phi = \frac{\sum_{i,j} |\phi(i,j,n) - \phi(i,j,n-1000)|^2}{\sum_{i,j} |\phi(i,j,n)|^2} < 1.0 \times 10^{-8}. \quad (37)$$

In our simulation, we iterate $n = 4 \times 10^5$ time steps for each case, and $\delta\Phi < 1.0 \times 10^{-9}$ for all the cases, which are more than one order of magnitude smaller than those in the literature.⁸ Therefore, the droplet is stable at this time. We plot the density profiles (Fig. 1) and the Young-Laplace law (Fig. 2) at this stable time. Our numerical results show good agreement with the analytical results. Fig. 2 also shows that our results are better than Yang *et al.*⁸'s large-density-ratio results without the WENO scheme. Yang *et al.*⁸ mentioned that the ratio of numerical surface tensions to analytical ones is about 96.5% in their results, while our results are around 99%. We note that $v^* = 1$ in Yang *et al.*⁸'s paper, not the same as the ratio between water and air. Zhang *et al.*⁴²'s Laplace law results utilizing Cahn-Hilliard model are also better than Yang *et al.*⁸'s comparing to the analytical result, but with a small density ratio $\rho^* = 5$.

B. 2D Rayleigh-Taylor instability

The Rayleigh–Taylor instability (RTI) occurs when a heavy fluid A is on top of a light fluid B , and is driven by the gravity. The heavy fluid falls into the light fluid and creates the instability between the fluid-fluid interface. The RTI is a common phenomenon, and it is also a classical benchmark problem widely simulated in the previous studies.^{6–8,42,43,50,54} We use RTI to test the ability to capture complex interface evolution at high Reynolds number and large density ratio for our DUGKS-PF(AC)-WENO approach.

The computational domain of 2D RTI in our simulation is $[0, 4L] \times [0, L]$ with $L = 256$. The reference velocity is $U_0 = \sqrt{gL}$. The order parameter, density, dynamic viscosity of the heavy fluid and light fluid are ϕ_A, ρ_A, μ_A and ϕ_B, ρ_B, μ_B , respectively. The main dimensionless numbers of this physical problem are the Atwood number $At = (\rho_A - \rho_B) / (\rho_A + \rho_B)$ and the Reynolds number $Re = \rho_A U_0 L / \mu_A$. Other dimensionless parameters are the capillary number $Ca = \mu_A U_0 / \sigma$, Peclet number $Pe = U_0 L / M_{AC}$, and the viscosity ratio. The reference time is defined as $T = \sqrt{\frac{L}{g \cdot At}}$,

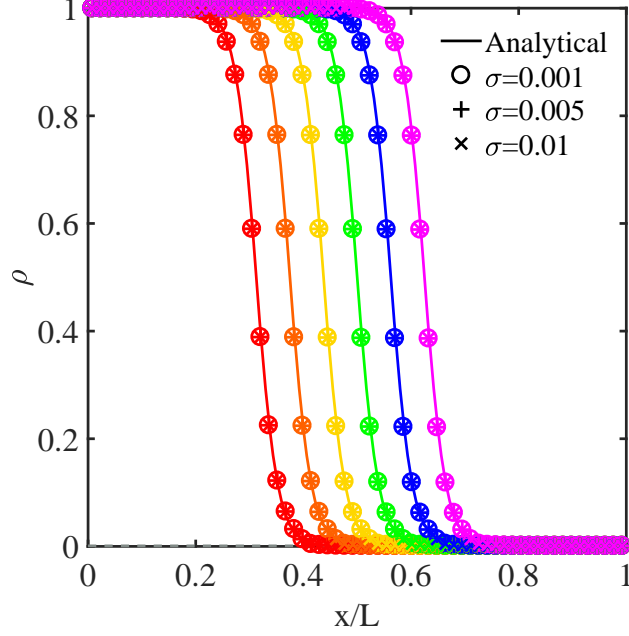


FIG. 1. The density profile of each stationary droplet at $\rho^* = 1000$ and $v^* = 0.06$. $R_0 = 20, 24, 28, 32, 36, 40$ from left to right. The gray dashed line represents the constant $\rho_B = 0.001$. The "Analytical" results are based on Eq. (36) and Eq. (11a) with different radii.

then the normalized time is $t^* = t/T$. The periodic boundary condition is applied to the lateral boundaries and the no-slip bounce-back boundary condition is applied to the top and bottom walls. Initially, the two-phase interface is located at

$$x(y) = 2L + 0.1L \cos\left(\frac{2\pi y}{L}\right). \quad (38)$$

First, we simulate a common high Reynolds number case, $At = 0.5$ and $Re = 3000$, which has been widely tested in the literatures.^{6-8,42,43,50} The other parameters in our simulation are $g = 2e-6$, $CFL = 0.25$, $\mu_A/\mu_B = 1.0$, $W = 5.0$, $Ca = 0.44$, $Pe = 1000$. The contours of the order parameter vary with the normalized time are shown in Fig. 3. It can be seen that the heavy fluid accelerates into the light fluid with a symmetric rolling-up process due to the gravitational field, and many small structures are generated at the later times. The evolution contours are in good agreement with the previous studies^{6-8,42,43,50} at the early times, but are not precisely the same at the later times because the small structures are sensitive to the minor differences in different methods. We compare the evolution of the positions of bubble front and spike tip with Chen *et al.* (2019),⁴³ as shown in Fig. 4. The results agree well with their results with two different approaches (DUGKS-PF(CH) and ARCHER). Since Chen *et al.* (2019)⁴³ have compared their results with the previous

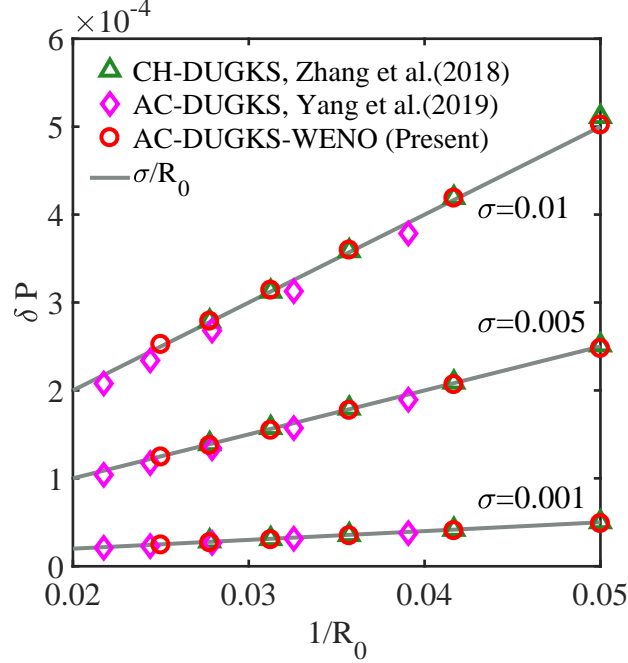


FIG. 2. Examination of the Laplace law for a stationary droplet. $(\rho^*, v^*) = (5, 1), (1000, 1), (1000, 0.06)$ in Zhang *et al.*⁴²'s paper, Yang *et al.*⁸'s paper, and our present simulation, respectively. $\delta P = \sigma/R_0$ is the analytical result of the 2D Laplace law, where $P = p + \phi d\psi/d\phi - \psi - \kappa\phi\nabla^2\phi - \kappa|\nabla\phi|^2/2 - \phi\mu_\phi$ in our simulation.

studies.^{50,55–57} Therefore, our results are also consistent with these previous results.

Next, a large density ratio of 1000 (or $At = 0.998$) and high Reynolds number ($Re = 3000$) case is carried out, which is a difficult case for the phase-field model.^{6,7} In our simulation, the other parameters are $U_0 = 0.02$, $CFL = 0.25$, $\mu_B/\mu_A = 2.0$, $W = 5.0$, $Ca = 0.44$, $Pe = 2000$. Fig. 5 shows the contours of ϕ at several normalized times. Since the density ratio is large, the influence of light fluid is small, hence the interface is smooth during the evolution process, and there is no rolling-up process and no small droplet structures. These qualitative features are in good agreement with the previous studies.^{6,7} For the positions of bubble front and spike tip at $At = 0.998$ and $Re = 3000$, we can only find one related paper (Kumar *et al.*⁷) and compare with them in Fig. 6. The results are also in reasonable agreement.

Yang *et al.*⁸ reported that they could not simulate a case with $At = 0.98$ and $Re = 600$ by the DUGKS-PF(AC) approach. Therefore, our approach with the WENO scheme can better model the larger density ratio and higher Reynolds number than theirs. Furthermore, they need a greater interfacial thickness $W = 8$ for the large density ratio RTI case, while we can apply the common

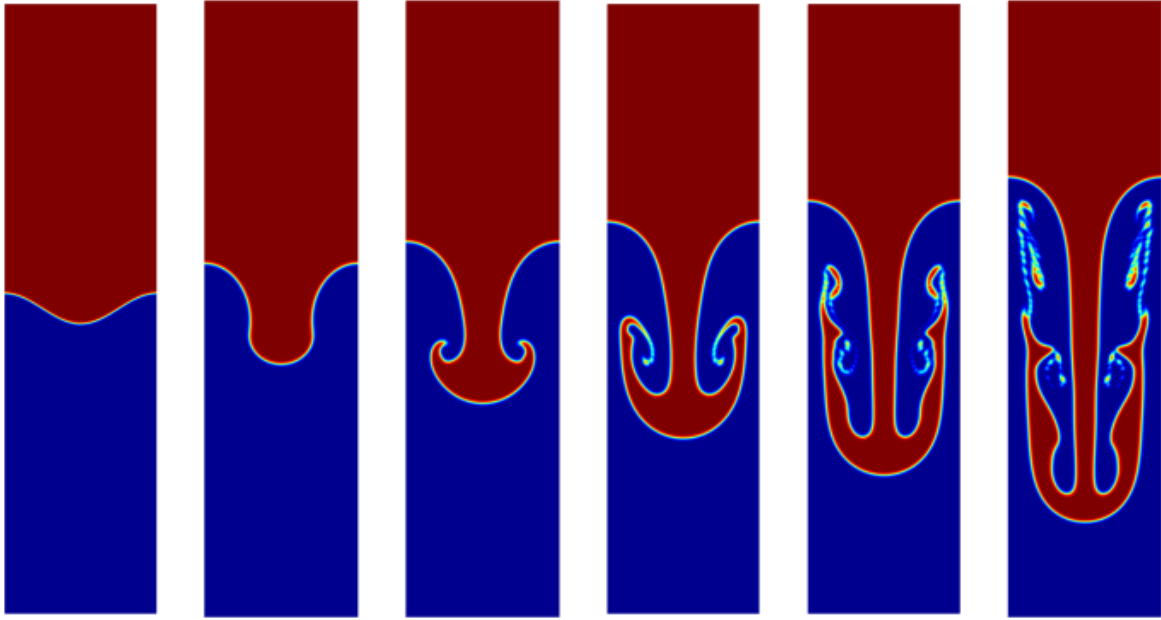


FIG. 3. Time evolution of ϕ for 2D RTI at $At = 0.5$ and $Re = 3000$. $t^* = 0, 1, 1.5, 2, 2.5, 3$.

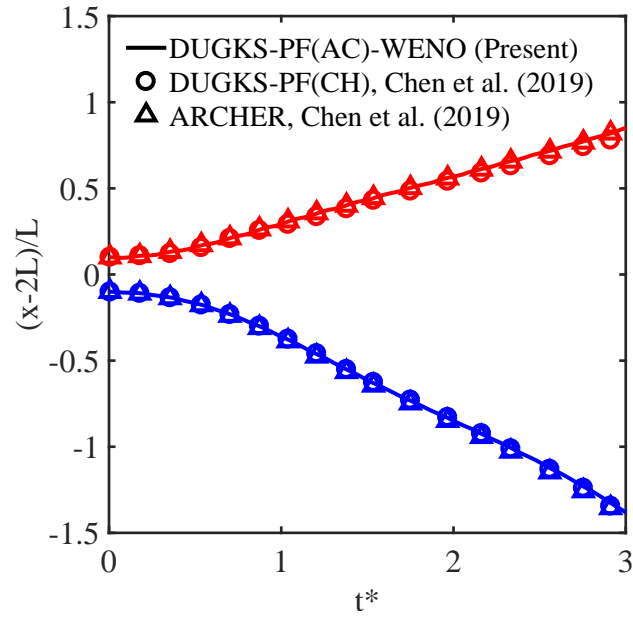


FIG. 4. Time evolution of the positions of bubble front (red) and spike tip (blue) for 2D RTI at $At = 0.5$ and $Re = 3000$.

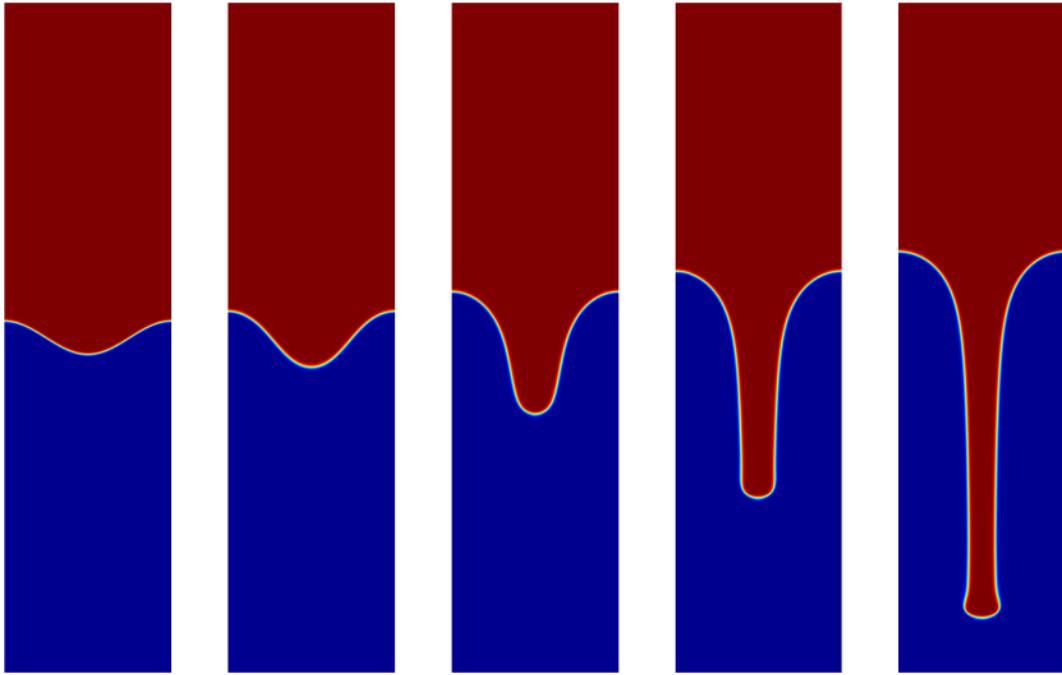


FIG. 5. Time evolution of ϕ for 2D RTI at $At = 0.998$ and $Re = 3000$. $t^* = 0, 0.5, 1, 1.5, 2$.

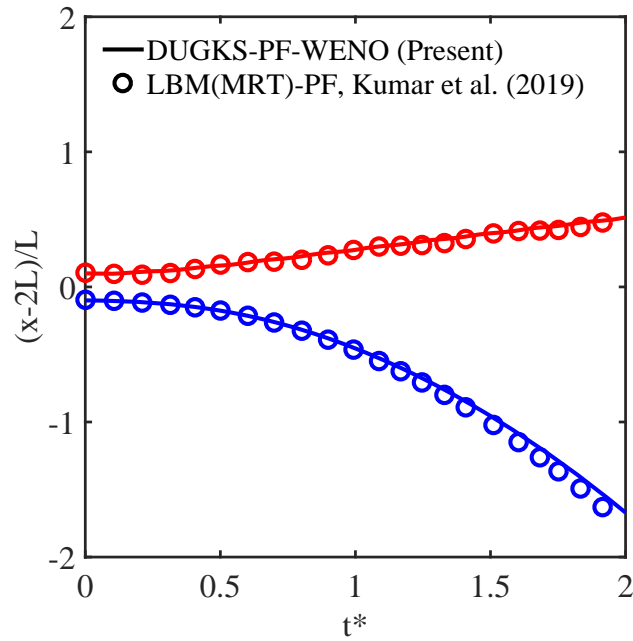


FIG. 6. Time evolution of the positions of bubble front (red) and spike tip (blue) for 2D RTI at $At = 0.998$ and $Re = 3000$.

value $W = 5$.

C. A droplet splashing on a thin liquid film

Droplet splashing occurs when the droplets fall down onto a wet ground, such as rain and shower. This physical problem is more challenge to simulate than RTI, because the initial droplet velocity is nonzero. The previous studies focus on the early stage of droplet impact on the liquid film.^{58–60} They found that there are two possible phenomena resulting from this impact process, deposition and splashing, mainly depending on the Reynolds number. Furthermore, when droplet splashing appears, the impact radius obeys a power law at this early stage.

The computational domain is 1024×512 . The periodic boundary condition is applied to the lateral boundaries and the no-slip bounce-back boundary condition is applied to the top and bottom walls. Initially, a circular liquid droplet with radius $R_0 = 64$ is on top of a thin liquid film with height $h = 32$. The droplet, with velocity magnitude $U_0 = 0.0102$, would fall down to the film. Gravity is not considered in this simulation. The interfacial thickness is $W = 5$. The mobility is $M_{AC} = 0.001$. The CFL number is still fixed at $CFL = 0.25$. The main dimensionless parameters are the Reynolds number $Re = 2R_0U_0/\nu_A$, Weber number $We = 2R_0\rho_A U_0^2/\sigma$, the density ratio $\rho^* = \rho_A/\rho_B$ and the kinematic viscosity ratio $\nu^* = \nu_A/\nu_B$. Here A represents the liquid phase (including the droplet and the thin film) and B is the background phase.

First, we model the deposition phenomenon. A small Reynolds number, $Re = 20$, is selected. Other dimensionless parameters are $We = 8000$, $\rho^* = 1000$, $\nu^* = 0.06$. The impact process is shown in Fig. 7. The droplet spreads gently on the film, and an outward moving surface wave is observed in this case, which is typical for the deposition process.^{58–60}

Then we simulate the splashing phenomenon. A large Reynolds number, $Re = 500$, is assumed in this case. Other dimensionless parameters are $We = 8000$, $\rho^* = 1000$, $\nu^* = 0.001$. The evolution of droplet splashing process is shown in Fig. 8. We can observe that two liquid fingers are generated after the impact of the droplet onto the thin film. In the end, the fingers may break up into small droplets, due to the Rayleigh–Plateau instability.^{58–60}

The evolution of spread factor r/D_0 is compared with Lee and Lin⁵⁹ in Fig. 9. Here the spread-radius r is defined as the radius of the position where the velocity magnitude has a maximum value in the whole domain.⁵⁸ Our results agrees well with the previous studies, and the power law evolution of the radius is reproduced, which demonstrates the ability of our approach.

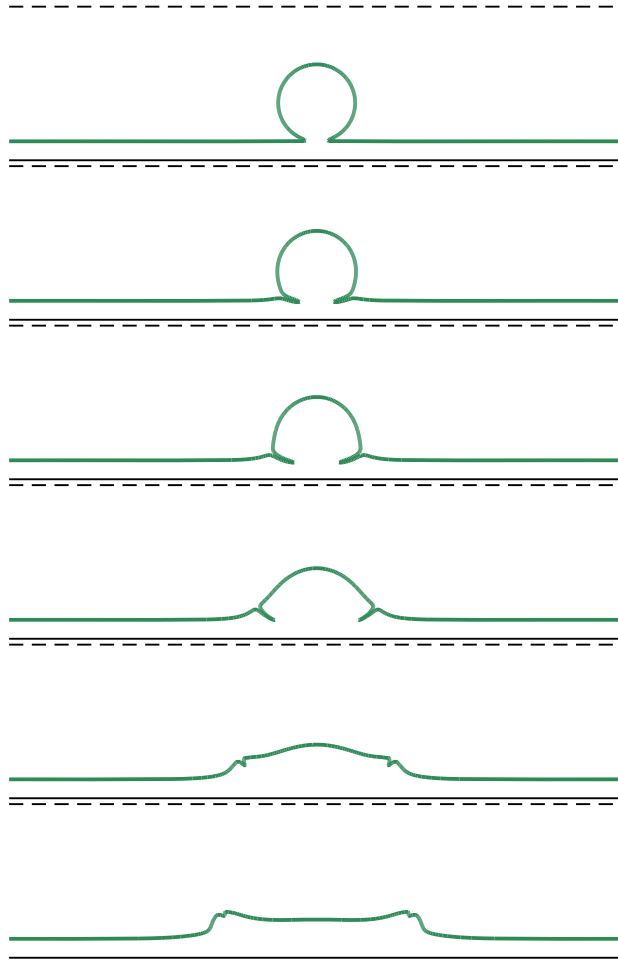


FIG. 7. Evolution of the fluid-fluid interface for a droplet splashing on a thin liquid film at $\rho^* = 1000$, $Re = 20$, and $We = 8000$. $U_0 t/D_0 = 0, 0.1, 0.2, 0.4, 0.8, 1.6$. The dashed line marks the centerline of the computational domain.

IV. THREE DIMENSIONAL SIMULATIONS AND DISCUSSIONS

Practical problems are mostly three dimensional, thus accurate simulation of 3D physical problems are needed. In this section, numerical simulations are carried out to model the 3D two-phase flow problems.

A. Collision of two droplets

The phenomenon of droplets collision appears widely in the nature and industry, such as raining, printing, and spray combustion. In this subsection, the collision of binary equal-sized droplets

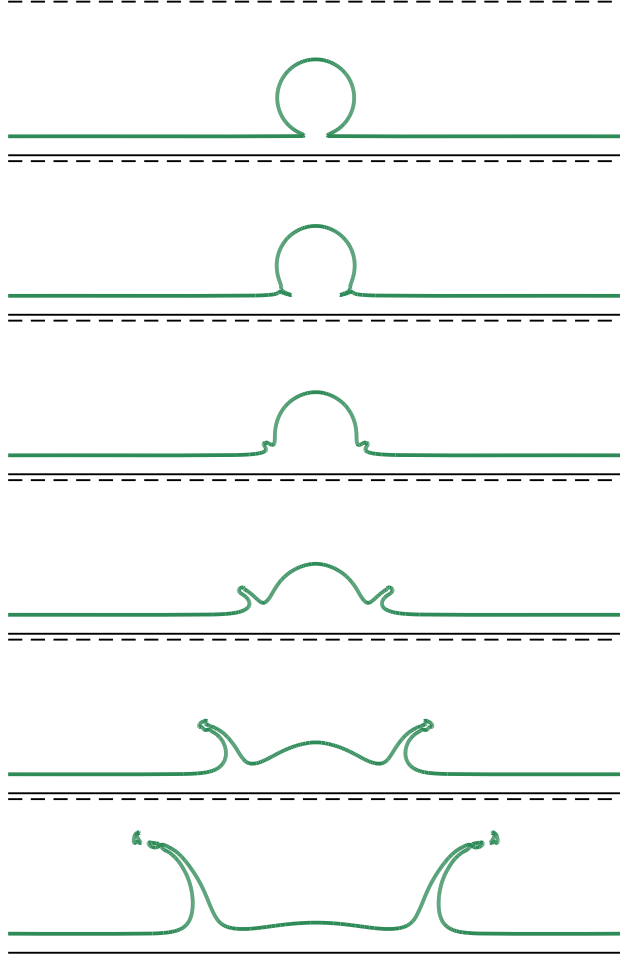


FIG. 8. Evolution of the fluid-fluid interface for a droplet splashing on a thin liquid film at $\rho^* = 1000$, $Re = 500$, and $We = 8000$. $U_0 t/D_0 = 0, 0.1, 0.2, 0.4, 0.8, 1.6$. The dashed line marks the centerline of the computational domain.

is modeled to demonstrate that our approach can capture well the dynamics of 3D droplets. Initially, two spherical droplets with radii $R_0 = 16$ are placed at the center line of the computational domain of size 128^3 . The distance of the centers of the two droplets is 48. The periodic boundary conditions are applied in all spatial directions. The main dimensionless parameters of this problem are the Reynolds number $Re = 2R_0U_0/v_A = 1720$, Weber number $We = 2R_0\rho_A U_0^2/\sigma = 58$, the density ratio $\rho^* = \rho_A/\rho_B$ and the kinematic viscosity ratio $\nu^* = \nu_A/\nu_B = 0.01$. Here A is the droplet phase and B is the background phase. The other parameters are $W = 5$, $M_{AC} = 0.01$, the acceleration of gravity $\mathbf{g} = 0$, and the initial relative velocity $U_0 = 0.02$. The pressure is initialized as $p = 2\phi\sigma/R_0$. The CFL number is still fixed at $CFL = 0.25$.

First, the density ratio is selected as $\rho^* = 1000$ to compare with the previous experimental

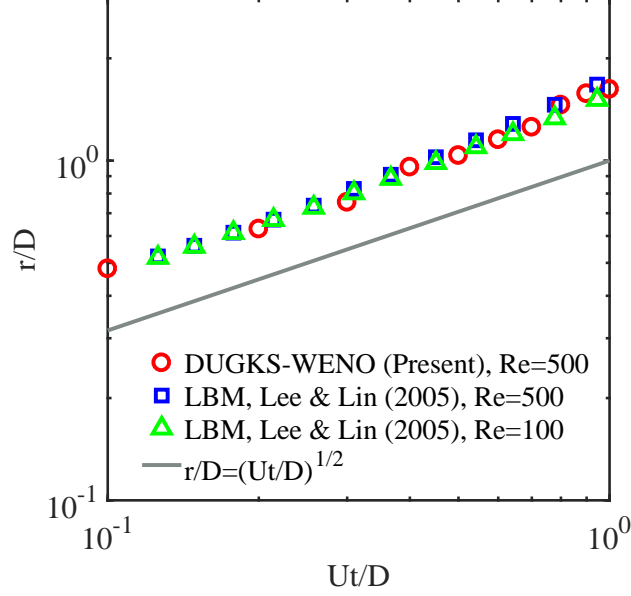


FIG. 9. Time evolution of the spread factor r/D_0 for 2D droplet splashing.

(Fig. 10) and numerical results.^{53,61} The droplets head-on collision dynamic for this case is shown in Fig. 11. At the beginning, the two droplets move towards each other and merge, like two hats that fit together. Then the hats flatten gradually by inertia. As mass is conserved, the brim thickens gradually. The center region thinned out so that a hole opens, the hats become a doughnut. The doughnut contracts to the center and the hole disappears due to surface tension. Again, because of inertia force and conserved mass, the large droplet elongates to the two sides in the initial droplets direction, and becomes a stick. As time proceeds, the center of the stick is stretched and eventually broken. One small satellite droplet is created in the end, which is also reported by Pan *et al.*⁶¹ experimentally (Fig. 10) and Lycett-Brown and Luo⁵³ numerically.

Second, we decrease the density ratio to see how it affects the droplets collision process. The interface dynamics of $\rho^* = 100, 10, 1$ are shown in Figs. 12-14, respectively. For the $\rho^* = 100$ case, the general evolution process is almost the same as the $\rho^* = 1000$ case, because the density of the background flow is so small that it can be neglected for these two cases. The main difference is that the satellite droplet is much smaller. For the $\rho^* = 10$ case, the density of the background flow cannot be neglected anymore. The impeding effect of background flow field on the droplets appears. Hence the droplets evolve slightly more slowly, as shown in Fig. 13, compared to Fig. 11 or Fig. 12. For instance, at $U_0 t / (2R_0) = 7.03$, the doughnut of the $\rho^* = 10$ case is larger than that of the $\rho^* = 1000$ or $\rho^* = 100$ case. This doughnut will become smaller due to the surface

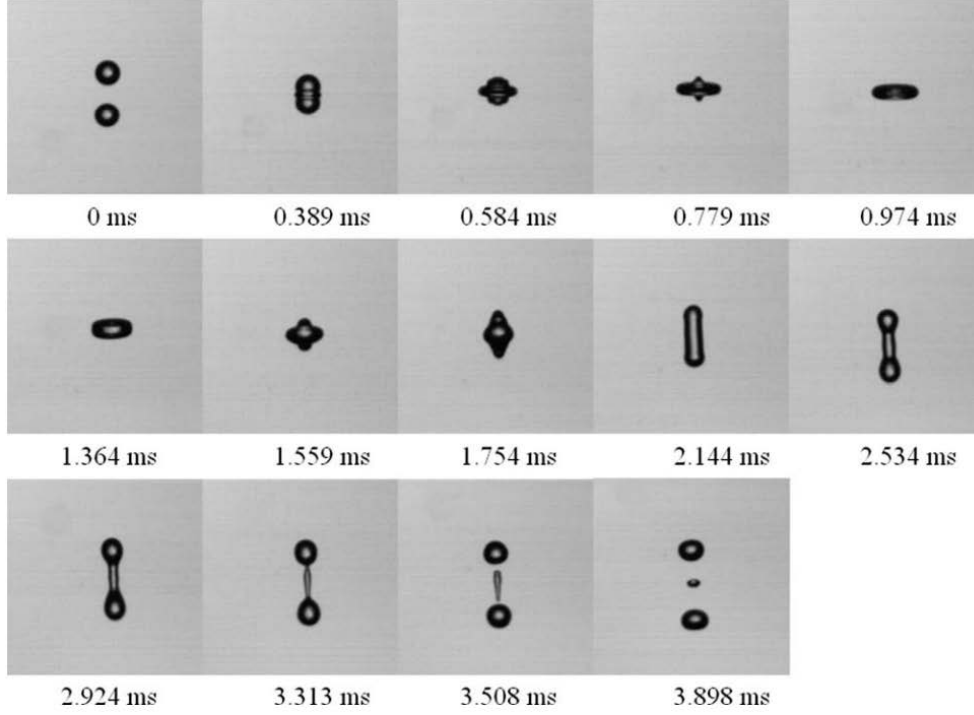


FIG. 10. Experimental results by Pan *et al.*⁶¹ for the head-on collisions of binary droplets, showing that a satellite droplet is formed between two large droplets. $Re = 1720$ and $We = 58$.

tension force. At $U_0 t / (2R_0) = 18.0$, the droplets are still connected with each other for the $\rho^* = 10$ case, while they have already separated for the larger-density-ratio cases. For the $\rho^* = 1$ case, the background flow field has obvious influence on the droplets dynamics. The droplets evolve more slowly and we show the large times of this same-density-ratio case (Figs. 14), compared to the above large density-ratio cases. One major difference for this case is that the droplet would not break up after collision. Should the simulation continues, only one large droplet would be present.

B. 3D Rayleigh-Taylor instability

In this subsection, 3D RTI is performed to further demonstrate the accuracy and stability of our DUGKS-PF(AC)-WENO approach in solving more complex interfacial flows. The computational domain is $[0, 4L] \times [0, L] \times [0, L]$ with $L = 128$. The boundary condition is periodic on the lateral boundaries, while the bounce-back scheme is implemented on the top and bottom walls. Initially, the two-phase interface is located at

$$x(y, z) = 2L + 0.05L \left[\cos\left(\frac{2\pi y}{L}\right) + \cos\left(\frac{2\pi z}{L}\right) \right]. \quad (39)$$

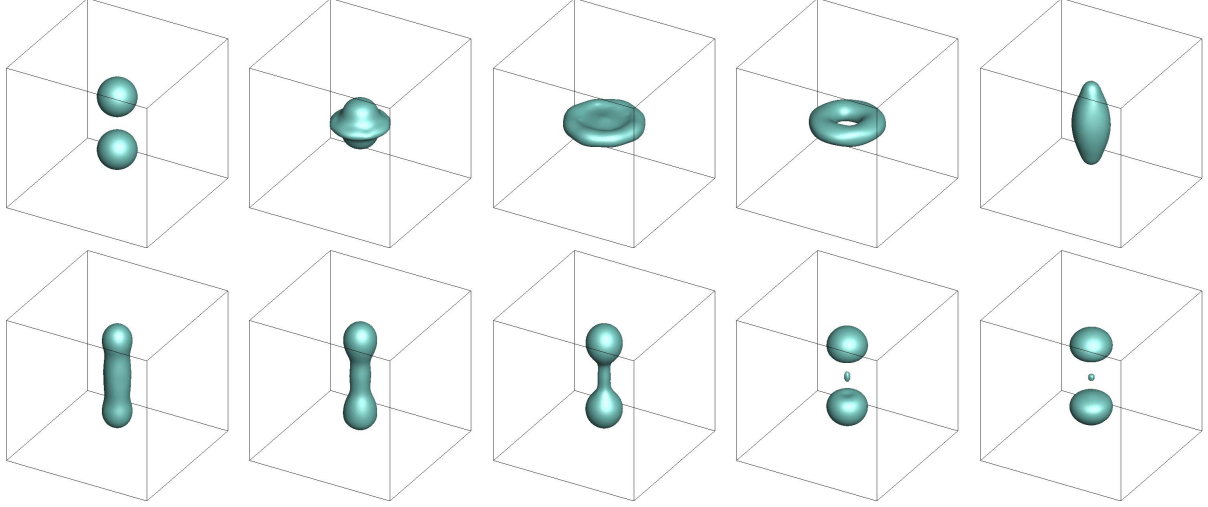


FIG. 11. Evolution of fluid-fluid interface for head-on collisions of binary droplets, showing that a satellite droplet is formed between the two droplets. $\rho^* = 1000$, $Re = 1720$, $We = 58$. $U_{0t}/(2R_0) = 0, 1.56, 3.13, 7.03, 10.2, 12.5, 14.8, 16.4, 18.0, 18.8$.

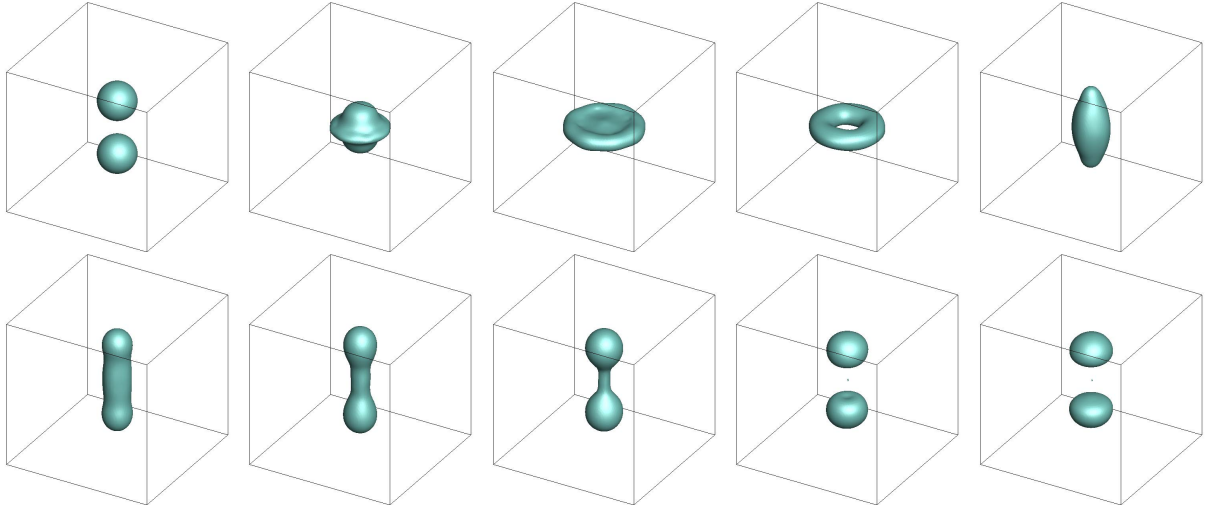


FIG. 12. Evolution of fluid-fluid interface for head-on collisions of binary droplets. A small satellite droplet is still formed in this case. $\rho^* = 100$, $Re = 1720$, $We = 58$. $U_{0t}/(2R_0) = 0, 1.56, 3.13, 7.03, 10.2, 12.5, 14.8, 16.4, 18.0, 18.8$.

The reference time is defined as $T = \sqrt{L/g}$ in the 3D RTI simulations, for a comparison with the results of He *et al.*⁶² and Wang *et al.*² The definitions of other parameters are the same as those in subsection III B.

To demonstrate the accuracy of our approach, a high Reynolds number case ($At = 0.5$ and $Re =$

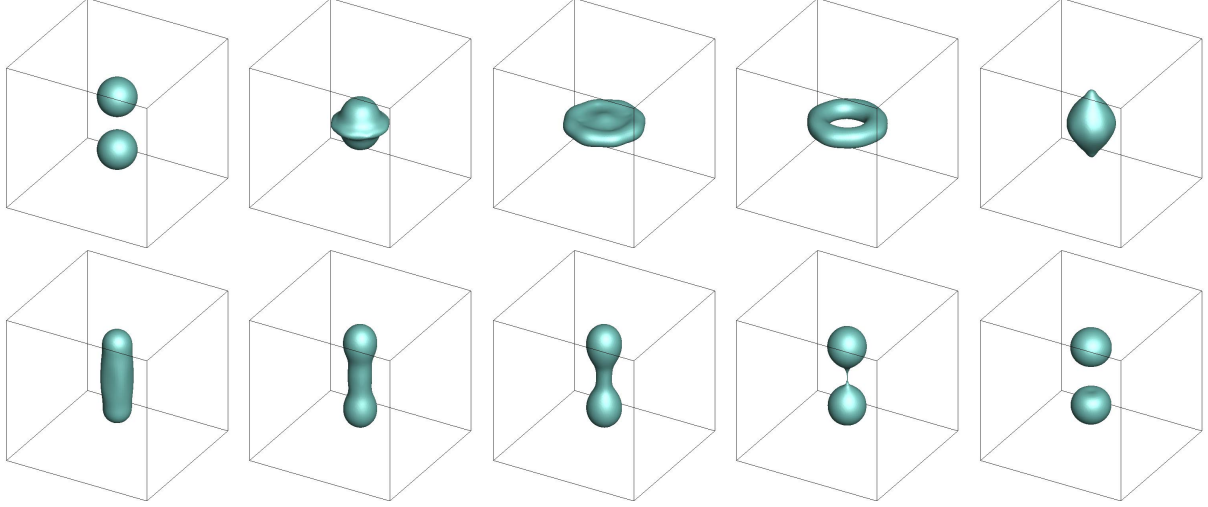


FIG. 13. Evolution of fluid-fluid interface for head-on collisions of binary droplets. $\rho^* = 10$, $Re = 1720$, $We = 58$. $U_0 t / (2R_0) = 0, 1.56, 3.13, 7.03, 10.2, 12.5, 14.8, 16.4, 18.0, 18.8$.

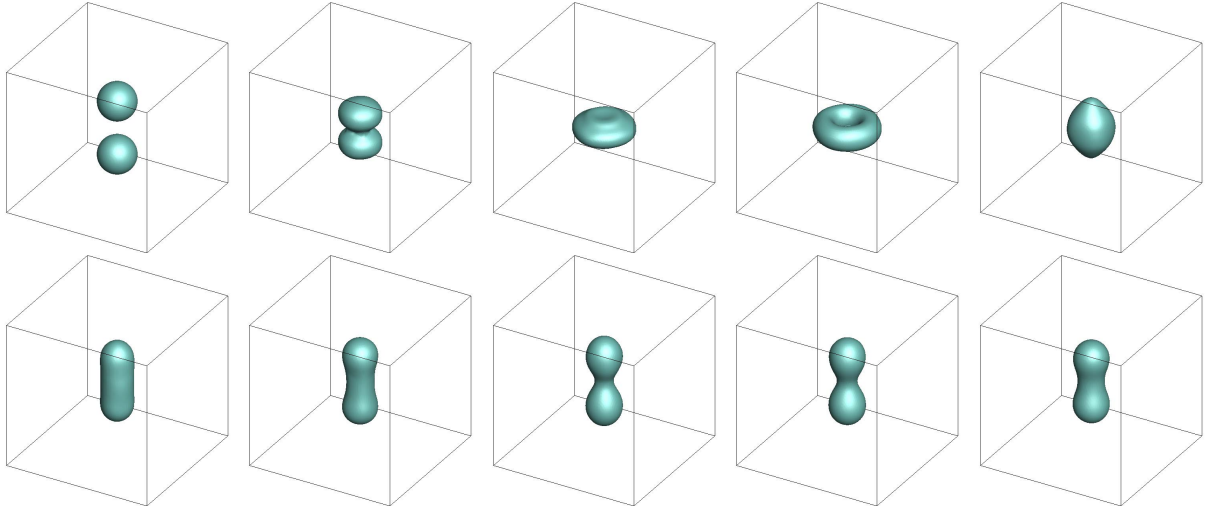


FIG. 14. Evolution of fluid-fluid interface for head-on collisions of binary droplets. $\rho^* = 1$, $Re = 1720$, $We = 58$. $U_0 t / (2R_0) = 0, 1.56, 3.13, 10.2, 13.3, 15.6, 17.2, 20.3, 21.9, 23.4$.

1024) is simulated to compare with the results from the literatures.^{2,62} Since He *et al.*⁶² did not consider surface tension and Wang *et al.*² did not mention surface tension in the 3D RTI simulation, we also choose a negligible surface tension such that the capillary number is $Ca = 1.5 \times 10^{15}$. The other parameters in our simulation are $U_0 = 0.02$, $CFL = 0.25$, $\mu_A / \mu_B = 3.0$, $W = 5.0$, $Pe = 20000$. The 3D interface evolution is shown in Fig. 15. Due to the local Kelvin–Helmholtz instability, the rolling-up processes and mushroom structures are observed. The profiles are almost the same as those reported by the previous studies using He-Chen-Zhang (HCZ) model (He *et al.*⁶²) and

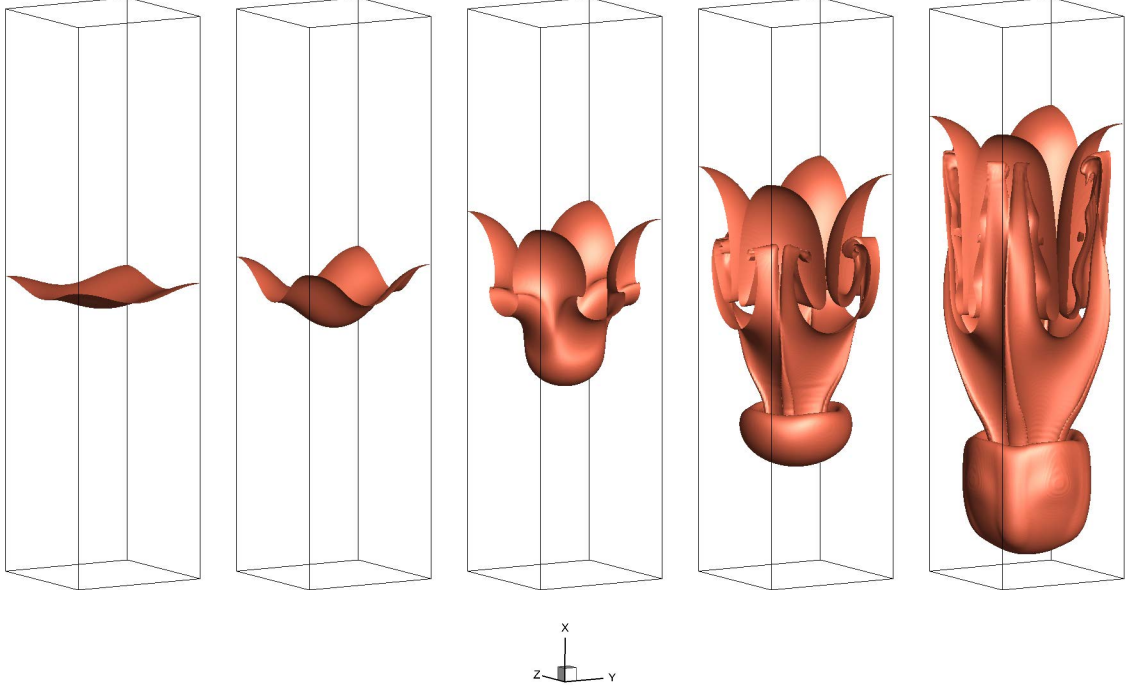


FIG. 15. Time evolution of fluid-fluid interface for 3D RTI at $At = 0.5$ and $Re = 1024$. $t^* = 0, 1, 2, 3, 4$.

multiphase lattice Boltzmann flux solver (MLBFS) method (Wang *et al.*²). We also compare the evolution of three main positions (bubble front, saddle point, and spike tip) with their data in Fig. 16 and the results show a very good agreement. For more details of the interface evolution, we plot the density contours in different horizontal planes at $t^* = 4$ (Fig. 17) to compare with He *et al.*⁶² The planes are labeled by k and the altitudes are $x = k/L$, respectively. The results are very similar to those shown in He *et al.*⁶² except for the small structures where $k < 100$, since the minor details in the numerical methods will affect the small structures of the interface.

To demonstrate the stability of our approach, a large density ratio and high Reynolds number case ($At = 0.998$ and $Re = 3000$) is simulated. The other parameters are $U_0 = 0.02$, $CFL = 0.25$, $\mu_B/\mu_A = 2.0$, $W = 5.0$, $Ca = 0.44$, $Pe = 1000$. The interface evolution, time evolution of three characteristic positions, and density contours on horizontal planes are shown in Figs. 18-20, respectively. Similar as the 2D large density ratio RTI case in subsection III B, the interface profiles are smooth because the light fluid has little effect on the heavy fluid at such a large density ratio. In this case, we could not find any previous study that simulated the 3D RTI at the same parameters, hence our results can serve as a benchmark for other researchers in the future.

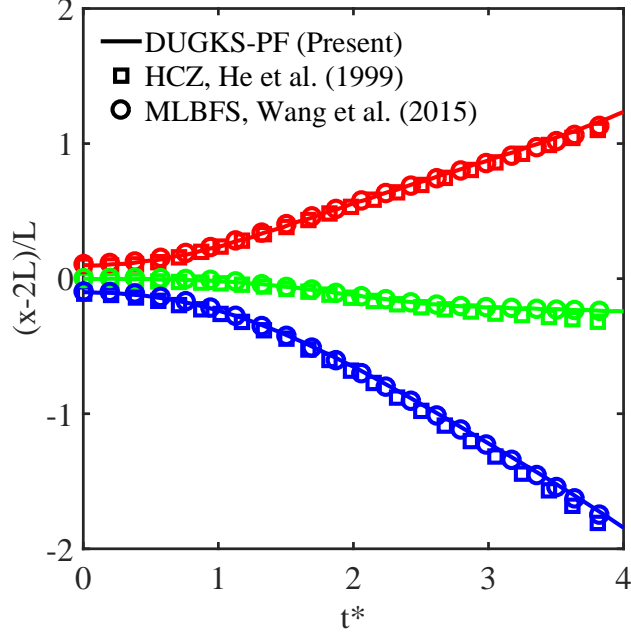


FIG. 16. Time evolution of the positions of bubble front (red), saddle point (green), and spike tip (blue) for 3D RTI at $At = 0.5$ and $Re = 1024$.

V. SUMMARY AND CONCLUSIONS

In this paper, a 3D DUGKS approach is developed, with two essential and logical improvements, in order to simulate the immiscible two-phase flows at large density ratios and high flow Reynolds numbers. For the two-phase model, the free-energy-based phase-field model is used. The evolution of order parameter satisfies the conservative Allen-Cahn equation, a second-order partial differential equation. To better reconstruct the particle distribution functions at cell interfaces and improve the numerical stability, a third-order weighted essentially non-oscillatory (WENO) scheme is applied.

Five benchmark problems are simulated to validate the PF(AC)-DUGKS-WENO code. For all the cases, the density ratio can reach $\rho^* \sim 1000$ without encountering numerical instability. For a 2D stationary droplet, the density profiles and the Young-Laplace law agree well with the analytical results, for different radii and different surface tensions. For 2D Rayleigh-Taylor instability, the evolution of the positions of bubble front and spike tip agrees well with the previous studies, and $Re \sim 3000$ is simulated to compare with the previous results when $\rho^* \sim 1000$. For a 2D droplet impacting on a thin liquid film, both the deposition phenomenon and splashing phenomenon are reproduced, and the evolution of the impact radius fits well with the literature data.

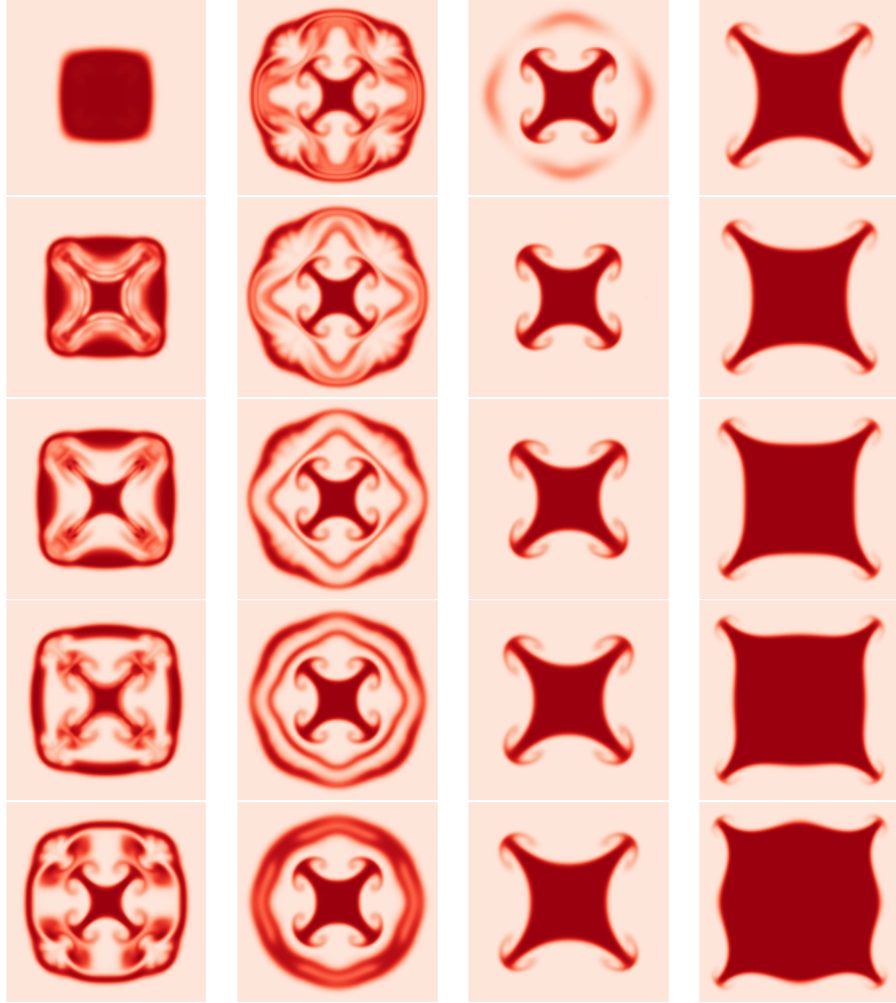


FIG. 17. Density contours in horizontal (y,z) planes for 3D RTI at $At = 0.5$ and $Re = 1024$. $t^* = 4$. $k = 30, 40, 50, 60, 70$ for the first column, $k = 80, 90, 100, 110, 120$ for the second column, $k = 130, 140, 150, 160, 170$ for the third column, $k = 180, 190, 200, 210, 220$ for the fourth column. The plane altitude is $x = k/128$.

For 3D binary-droplet collision, the evolution process of fluid-fluid interface at $\rho^* \sim 1000$ is very similar to the previous experimental result, and a small satellite droplet is reproduced between the two droplets. This case involves merging of two interfaces as well as breakup at different times. Furthermore, we studied how the density ratio affect the collision and breakup processes. When ρ^* becomes smaller, the satellite droplet is found to be also smaller. When $\rho^* \sim 1$, the two droplets would not break up in the end, due to the strong damping effect of background flow field.

For the case of 3D Rayleigh-Taylor instability, the evolution of the positions of bubble front, saddle point and spike tip at a density ratio of 3 agrees well with the results from previous studies.

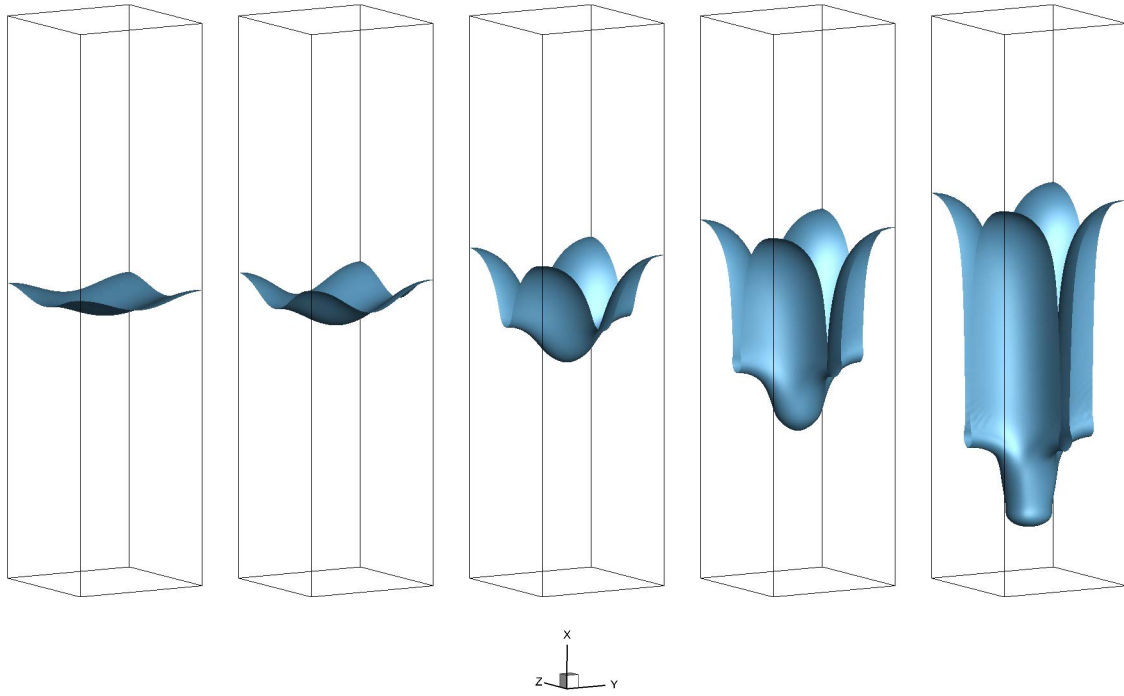


FIG. 18. Time evolution of fluid-fluid interface for 3D RTI at $At = 0.998$ and $Re = 3000$. $t^* = 0, 0.5, 1, 1.5, 2$.

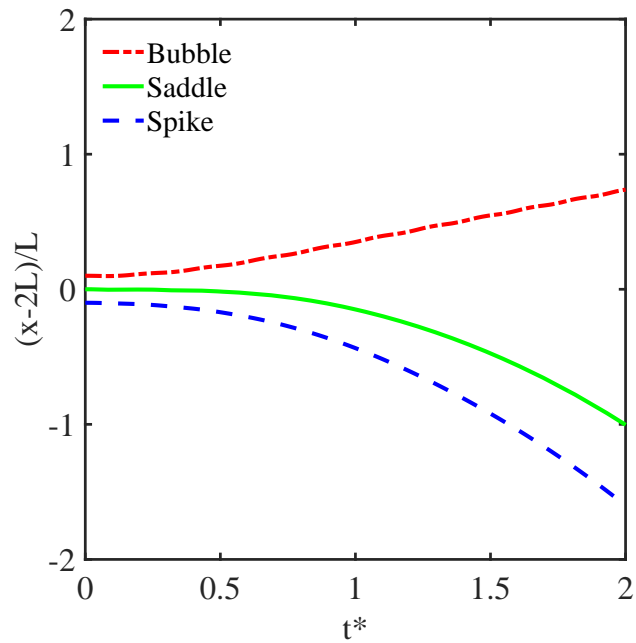


FIG. 19. Time evolution of the positions of bubble front, saddle point, and spike tip for 3D RTI at $At = 0.998$ and $Re = 3000$.



FIG. 20. Density contours in horizontal (y, z) planes for 3D RTI at $At = 0.998$ and $Re = 3000$. $t^* = 2$. $k = 60, 120, 180, 240, 300$. The plane altitude is $x = k/128$.

The density contours on the horizontal planes are also similar as those in the previous results. We then simulated the 3D case with $\rho^* = 1000$ and $Re = 3000$. To our knowledge, this is the first 3D simulation of RTI at such high levels of density ratio and Reynolds number, and these results could serve as a benchmark for future 3D studies.

Compared to Yang *et al.*⁸'s result, PF(AC)-DUGKS coupled with the WENO scheme is numerically more stable, which can simulate multiphase flows at larger density ratios and higher Reynolds numbers. Furthermore, we extend the method to 3D problems, and the results agree well with the experimental results. Hence our improved DUGKS approach makes the DUGKS scheme more capable in dealing with the realistic two-phase flow problems.

ACKNOWLEDGMENTS

This work has been supported by the National Natural Science Foundation of China (NSFC award numbers 91852205, 91741101 & 11961131006), NSFC Basic Science Center Program (Award number 11988102), the National Numerical Wind Tunnel program, the Taizhou-Shenzhen Innovation Center, Guangdong Provincial Key Laboratory of Turbulence Research and Applications (2019B21203001), Guangdong-Hong Kong-Macao Joint Laboratory for Data-Driven Fluid Mechanics and Engineering Applications (2020B1212030001) and Shenzhen Science and Technology Program (Grant No. KQTD20180411143441009). Computing resources are provided by the Center for Computational Science and Engineering of Southern University of Science and Technology.

DATA AVAILABILITY

The data that support the findings of this study are available from the corresponding author upon reasonable request.

Appendix A: Integral constraints of the model Boltzmann equations for the ACNS system based on the Chapman-Enskog analysis

The purpose of this appendix is to derive the moment-integral constraints for f^{eq} , g^{eq} , S_α^f , and S_α^g in the model Boltzmann equations, *i.e.*, Eqs. (13a-13b), in order to recover the ACNS system, Eqs. (10a-10c). In particular, Eq. (13a) is applied to reproduce the conservative AC equation, Eq. (10a), while Eq. (13b) is applied to reproduce the hydrodynamic equations, Eqs. (10b) and (10c). Here f represents the distribution function for order parameter and g the distribution function for velocity/pressure. The density is obtained from order parameter by a linear relationship.

To reproduce the conservative AC equation, we take the zeroth-order moment of Eq. (13a) as

$$\int \left[\frac{\partial f}{\partial t} + \xi_m \frac{\partial f}{\partial x_m} = -\frac{f - f^{eq}}{\tau_f} + S^f \right] d\xi. \quad (\text{A1})$$

Comparing to Eq. (10a), we can define

$$\phi = \int f d\xi. \quad (\text{A2})$$

The collision operator in Eq. (13a) needs to conserve the order parameter, hence the zeroth-order moment of f^{eq} is

$$\int f^{eq} d\xi = \phi. \quad (\text{A3})$$

Furthermore, to obtain the mean advection term, the first-order moment of f^{eq} is chosen to yield

$$\int f^{eq} \xi_j d\xi = \phi u_j. \quad (\text{A4})$$

Then Eq. (A1) becomes

$$\frac{\partial \phi}{\partial t} + \frac{\partial}{\partial x_m} (\phi u_m) = \int S^f d\xi - \frac{\partial}{\partial x_m} \int (f - f^{eq}) \xi_m d\xi. \quad (\text{A5})$$

Using the Chapman-Enskog expansion, we have

$$\begin{aligned}
& \int (f - f^{eq}) \xi_j d\xi \\
&= -\tau_f \left[\frac{\partial}{\partial t} \int f^{eq} \xi_j d\xi + \frac{\partial}{\partial x_n} \int f^{eq} \xi_n \xi_j d\xi - \int S^f \xi_j d\xi \right] + \mathcal{O}(\tau_f^2) \\
&= -\tau_f \left[\frac{\partial}{\partial t} (\phi u_j) + \frac{\partial}{\partial x_n} \int f^{eq} \xi_n \xi_j d\xi - \int S^f \xi_j d\xi \right] + \mathcal{O}(\tau_f^2).
\end{aligned} \tag{A6}$$

Substituting Eq. (A6) into Eq. (A5) and compared with Eq. (10a), the following integral condition is required,

$$\begin{aligned}
& \int S^f d\xi + \frac{\partial}{\partial x_m} \left\{ \tau_f \left[\frac{\partial}{\partial t} (\phi u_m) + \frac{\partial}{\partial x_n} \int f^{eq} \xi_n \xi_m d\xi - \int S^f \xi_m d\xi \right] \right\} \\
& \sim \frac{\partial}{\partial x_m} \left[M_{AC} \left(\frac{\partial \phi}{\partial x_m} - \theta n_m \right) \right].
\end{aligned} \tag{A7}$$

In order to match the arrangement of spatial derivatives on the two sides, a convenient choice to accommodate Eq. (A7) is that

$$\int S^f d\xi = 0, \tag{A8a}$$

$$\frac{\partial}{\partial x_n} \int f^{eq} \xi_n \xi_m d\xi - \int S^f \xi_m d\xi = \frac{M_{AC}}{\tau_f} \left(\frac{\partial \phi}{\partial x_m} - \theta n_m \right) - \frac{\partial}{\partial t} (\phi u_m), \tag{A8b}$$

where $M_{AC}/\tau_f = RT = \text{const.}$ in this model. Similarly, one possible choice for Eq. (A8b) is

$$\int f^{eq} \xi_n \xi_m d\xi = RT \phi \delta_{nm}, \tag{A9a}$$

$$\int S^f \xi_m d\xi = RT \theta n_m + \frac{\partial}{\partial t} (\phi u_m). \tag{A9b}$$

We comment that the time derivative term can be converted to spatial derivative terms via the $\mathcal{O}(1)$ Euler-like equations, but it is not possible here to convert this to a clean form like $\partial A_{mn}/\partial x_n$. If the latter were possible, then the time derivative term could be merged into the second-order moment of f^{eq} to eliminate the derivative calculation.

To recover the continuity equation for incompressible flow, we take the zeroth-order moment of Eq. (13b) as

$$\int \left[\frac{\partial g}{\partial t} + \xi_m \frac{\partial g}{\partial x_m} = -\frac{g - g^{eq}}{\tau_g} + S^g \right] d\xi. \tag{A10}$$

As usual, the velocity field is obtained by

$$\rho u_j = \int g \xi_j d\xi. \tag{A11}$$

Compared to the velocity-divergence-free condition, Eq. (10b), and assuming the conservation condition of the collision operator, the following integral condition is derived

$$\int S^g d\xi - \frac{\partial}{\partial t} \int g d\xi = u_m \frac{\partial \rho}{\partial x_m}. \quad (\text{A12})$$

A logical choice is then

$$0 = \int g d\xi = \int g^{eq} d\xi, \quad (\text{A13a})$$

$$\int S^g d\xi = u_m \frac{\partial \rho}{\partial x_m}. \quad (\text{A13b})$$

Next, the first-order moment of Eq. (13b) is needed to recover the momentum equation, *i.e.*,

$$\int \left[\frac{\partial g}{\partial t} + \xi_m \frac{\partial g}{\partial x_m} = -\frac{g - g^{eq}}{\tau_g} + S^g \right] \xi_j d\xi. \quad (\text{A14})$$

Again, considering the conservation of collision operator, then Eq. (A11) implies that

$$\int g^{eq} \xi_j d\xi = \rho u_j. \quad (\text{A15})$$

With the above results, Eq. (A14) can be written as

$$\begin{aligned} & \frac{\partial}{\partial t} (\rho u_j) + \frac{\partial}{\partial x_k} \int g^{eq} \xi_j \xi_k d\xi \\ &= 0 + \int S^g \xi_j d\xi - \frac{\partial}{\partial x_k} \int (g - g^{eq}) \xi_j \xi_k d\xi \\ &= \int S^g \xi_j d\xi + \mathcal{O}(\tau_g). \end{aligned} \quad (\text{A16})$$

It is well known that $\mu \sim \mathcal{O}(\tau_g)$ in the mesoscopic approach. Then, to the leading-order, Eq. (10c) can be written as

$$\frac{\partial(\rho \mathbf{u})}{\partial t} + \nabla \cdot (\rho \mathbf{u} \mathbf{u}) = -\nabla p + \mathbf{F} + \mathcal{O}(\tau_g). \quad (\text{A17})$$

Comparing to Eq. (A17), a natural choice of Eq. (A16) is that the source term provides the external force, while the equilibrium distribution function provides the spatial-derivative terms, *i.e.*,

$$\int g^{eq} \xi_j \xi_k d\xi = \rho u_j u_k + p \delta_{jk}, \quad \int S^g \xi_j d\xi = F_j. \quad (\text{A18})$$

The $\mathcal{O}(\tau_g)$ term needs to recover the viscous term in Eq. (10c), *i.e.*,

$$\int (g - g^{eq}) \xi_j \xi_k d\xi \sim \left\{ -\mu \left(\frac{\partial u_j}{\partial x_k} + \frac{\partial u_k}{\partial x_j} \right) \right\}. \quad (\text{A19})$$

Using the Chapman-Enskog expansion, we have

$$\begin{aligned}
& \int (g - g^{eq}) \xi_j \xi_k d\xi \\
&= -\tau_g \left[\frac{\partial}{\partial t} \int g^{eq} \xi_j \xi_k d\xi + \frac{\partial}{\partial x_m} \int g^{eq} \xi_m \xi_j \xi_k d\xi - \int S^g \xi_j \xi_k d\xi \right] + \mathcal{O}(\tau_g^2) \\
&= -\tau_g \left[\frac{\partial}{\partial t} (\rho u_k u_j + p \delta_{kj}) + \frac{\partial}{\partial x_m} \int g^{eq} \xi_m \xi_j \xi_k d\xi - \int S^g \xi_j \xi_k d\xi \right] + \mathcal{O}(\tau_g^2).
\end{aligned} \tag{A20}$$

To proceed further, we need to approximate the time derivatives of the macroscopic variables. Since $M_{AC} \sim \mathcal{O}(\tau_f)$, Eq. (12) can be written as

$$\frac{\partial \rho}{\partial t} + \nabla \cdot (\rho \mathbf{u}) = \mathcal{O}(\tau_f). \tag{A21}$$

From Eq. (A21), Eq. (A17) and Eq. (10b), the evolution of density and velocity can be expressed as

$$\frac{\partial \rho}{\partial t} = -u_m \frac{\partial \rho}{\partial x_m} + \mathcal{O}(\tau_f), \tag{A22a}$$

$$\frac{\partial u_j}{\partial t} = -u_m \frac{\partial u_j}{\partial x_m} - \frac{1}{\rho} \frac{\partial p}{\partial x_j} + \frac{F_j}{\rho} + \mathcal{O}(\tau_g) + \mathcal{O}(\tau_f Ma). \tag{A22b}$$

Hence the time derivative terms in Eq. (A20) can be converted to

$$\begin{aligned}
& \frac{\partial}{\partial t} (\rho u_k u_j + p \delta_{kj}) \\
&= u_k u_j \frac{\partial \rho}{\partial t} + \rho u_j \frac{\partial u_k}{\partial t} + \rho u_k \frac{\partial u_j}{\partial t} + \frac{\partial p}{\partial t} \delta_{kj} \\
&= u_j F_k + u_k F_j + \mathcal{O}(\tau_f Ma^2, \tau_g Ma, Ma^2).
\end{aligned} \tag{A23}$$

In the above, the time derivative of the pressure term is assumed to scale as $\mathcal{O}(Ma^2)$, which applies for the regions outside the fluid-fluid interfaces. However, within the interfaces, due to the interface advection, $\partial p / \partial t \sim u_l \sigma / (WR)$, where u_l is the fluid velocity at the interface. Therefore, it follows that a condition $\sigma / W < \rho u^2$ would be required for dynamic interface problems.

Substituting Eq. (A23) into Eq. (A20), then Eq. (A19) yields the following moment-integral condition

$$\begin{aligned}
& \frac{\partial}{\partial x_m} \int g^{eq} \xi_m \xi_j \xi_k d\xi - \int S^g \xi_j \xi_k d\xi \\
& \sim \left\{ \frac{\mu}{\tau_g} \left(\frac{\partial u_j}{\partial x_k} + \frac{\partial u_k}{\partial x_j} \right) - u_j F_k - u_k F_j \right\}.
\end{aligned} \tag{A24}$$

Given the specific truncated form of the equilibrium g^{eq} , we have

$$\int g^{eq} \xi_m \xi_j \xi_k d\xi = \rho RT (u_k \delta_{mj} + u_j \delta_{mk} + u_m \delta_{jk}), \tag{A25}$$

then we obtain

$$\int S^g \xi_j \xi_k d\xi = u_j F_k + u_k F_j + RT \left(u_j \frac{\partial \rho}{\partial x_k} + u_k \frac{\partial \rho}{\partial x_j} + \delta_{jk} u_m \frac{\partial \rho}{\partial x_m} \right). \quad (\text{A26})$$

Certainly, this is only one of the many possible combinations of the third-order moment of g^{eq} and the second-order moment of S^g .

To summarize, the moment-integral constraints for the model Boltzmann equations are:

1. The conservative AC equation constrains to the zeroth-, first-, and second-order moments of f^{eq} , Eqs. (A3), (A4) and (A9a), and the zeroth- and first-order moments for S^f , Eqs. (A8a) and (A9b);
2. The continuity equation sets the zeroth-order moment for g^{eq} , Eq. (A13a) and the zeroth-order moment for S^g , Eq. (A13b);
3. The momentum equation provides the first-, second- and third-order moments for g^{eq} , first-order and second-order moments for S^g , *i.e.*, Eq. (A15), Eq. (A18), and Eq. (A24).

We point out that the above integral conditions are designed as one of the many possibilities. Furthermore, even with this design stated by the above integral constraints, there are many ways to specify the precise forms for f^{eq} , g^{eq} , S^f , and S^g . We can confirm that the specific forms given in Eqs. (14) and (15) do satisfy all the requirements stated above. We can also introduce other specific forms, for example, utilizing the Hermite expansion formulae, as done by Chen *et al.*⁶³ Eqs. (14) and (15) are used in our large-density-ratio simulations, because their capability have been verified by Yang *et al.*,⁸ and we combine the WENO treatment to improve the numerical stability of the PF(AC)-DUGKS approach.

REFERENCES

- ¹Y. Wang, C. Shu, H. Huang, and C. Teo, “Multiphase lattice Boltzmann flux solver for incompressible multiphase flows with large density ratio,” *Journal of Computational Physics* **280**, 404–423 (2015).
- ²Y. Wang, C. Shu, and L. Yang, “An improved multiphase lattice Boltzmann flux solver for three-dimensional flows with large density ratio and high Reynolds number,” *Journal of Computational Physics* **302**, 41–58 (2015).

- ³Z. Chen, C. Shu, D. Tan, X. D. Niu, and Q. Z. Li, “Simplified multiphase lattice Boltzmann method for simulating multiphase flows with large density ratios and complex interfaces,” *Phys. Rev. E* **98**, 063314 (2018).
- ⁴H. Liang, J. Xu, J. Chen, H. Wang, Z. Chai, and B. Shi, “Phase-field-based lattice Boltzmann modeling of large-density-ratio two-phase flows,” *Phys. Rev. E* **97**, 033309 (2018).
- ⁵H. Liang, H. Liu, Z. Chai, and B. Shi, “Lattice Boltzmann method for contact-line motion of binary fluids with high density ratio,” *Phys. Rev. E* **99**, 063306 (2019).
- ⁶A. Fakhari, T. Mitchell, C. Leonardi, and D. Bolster, “Improved locality of the phase-field lattice-Boltzmann model for immiscible fluids at high density ratios,” *Phys. Rev. E* **96**, 053301 (2017).
- ⁷E. D. Kumar, S. A. Sannasiraj, and V. Sundar, “Phase field lattice Boltzmann model for air-water two phase flows,” *Physics of Fluids* **31**, 072103 (2019).
- ⁸Z. Yang, C. Zhong, and C. Zhuo, “Phase-field method based on discrete unified gas-kinetic scheme for large-density-ratio two-phase flows,” *Phys. Rev. E* **99**, 043302 (2019).
- ⁹Z. Yang, S. Liu, C. Zhuo, and C. Zhong, “Conservative multilevel discrete unified gas kinetic scheme for modeling multiphase flows with large density ratios,” *Physics of Fluids* **34**, 043316 (2022).
- ¹⁰D. Juric and G. Tryggvason, “A Front-Tracking Method for Dendritic Solidification,” *Journal of Computational Physics* **123**, 127–148 (1996).
- ¹¹R. Scardovelli and S. Zaleski, “DIRECT NUMERICAL SIMULATION OF FREE-SURFACE AND INTERFACIAL FLOW,” *Annual Review of Fluid Mechanics* **31**, 567–603 (1999).
- ¹²N. Balcázar, O. Lehmkuhl, L. Jofre, J. Rigola, and A. Oliva, “A coupled volume-of-fluid/level-set method for simulation of two-phase flows on unstructured meshes,” *Computers and Fluids* **124**, 12–29 (2016).
- ¹³M. Sussman, E. Fatemi, P. Smereka, and S. Osher, “An improved level set method for incompressible two-phase flows,” *Computers and Fluids* **27**, 663–680 (1998).
- ¹⁴H. Liu, A. J. Valocchi, and Q. Kang, “Three-dimensional lattice Boltzmann model for immiscible two-phase flow simulations,” *Phys. Rev. E* **85**, 046309 (2012).
- ¹⁵A. K. Gunstensen, D. H. Rothman, S. Zaleski, and G. Zanetti, “Lattice Boltzmann model of immiscible fluids,” *Phys. Rev. A* **43**, 4320–4327 (1991).
- ¹⁶X. Shan and H. Chen, “Lattice Boltzmann model for simulating flows with multiple phases and components,” *Phys. Rev. E* **47**, 1815–1819 (1993).

- ¹⁷X. Shan and H. Chen, “Simulation of nonideal gases and liquid-gas phase transitions by the lattice Boltzmann equation,” *Phys. Rev. E* **49**, 2941–2948 (1994).
- ¹⁸M. R. Swift, E. Orlandini, W. R. Osborn, and J. M. Yeomans, “Lattice Boltzmann simulations of liquid-gas and binary fluid systems,” *Phys. Rev. E* **54**, 5041–5052 (1996).
- ¹⁹D. H. Rothman and J. M. Keller, “Immiscible cellular-automaton fluids,” *Journal of Statistical Physics* **52**, 1119–1127 (1988).
- ²⁰S. Chen and G. D. Doolen, “LATTICE BOLTZMANN METHOD FOR FLUID FLOWS,” *Annual Review of Fluid Mechanics* **30**, 329–364 (1998).
- ²¹Y. Ba, H. Liu, Q. Li, Q. Kang, and J. Sun, “Multiple-relaxation-time color-gradient lattice Boltzmann model for simulating two-phase flows with high density ratio,” *Phys. Rev. E* **94**, 023310 (2016).
- ²²Q. Li, K. H. Luo, and X. J. Li, “Lattice Boltzmann modeling of multiphase flows at large density ratio with an improved pseudopotential model,” *Phys. Rev. E* **87**, 053301 (2013).
- ²³C. Zhang, Z. Guo, and Y. Li, “A fractional step lattice Boltzmann model for two-phase flow with large density differences,” *International Journal of Heat and Mass Transfer* **138**, 1128–1141 (2019).
- ²⁴Y.-H. Qian, D. d’Humières, and P. Lallemand, “Lattice BGK models for Navier-Stokes equation,” *EPL (Europhysics Letters)* **17**, 479 (1992).
- ²⁵S. M. Allen and J. W. Cahn, “Mechanisms of phase transformations within the miscibility gap of Fe-rich Fe-Al alloys,” *Acta Metallurgica* **24**, 425–437 (1976).
- ²⁶Y. Sun and C. Beckermann, “Sharp interface tracking using the phase-field equation,” *Journal of Computational Physics* **220**, 626–653 (2007).
- ²⁷P.-H. Chiu and Y.-T. Lin, “A conservative phase field method for solving incompressible two-phase flows,” *Journal of Computational Physics* **230**, 185–204 (2011).
- ²⁸J. W. Cahn and J. E. Hilliard, “Free energy of a nonuniform system. I. Interfacial free energy,” *The Journal of chemical physics* **28**, 258–267 (1958).
- ²⁹J. W. Cahn and J. E. Hilliard, “Free energy of a nonuniform system. III. Nucleation in a two-component incompressible fluid,” *The Journal of chemical physics* **31**, 688–699 (1959).
- ³⁰H. L. Wang, Z. H. Chai, B. C. Shi, and H. Liang, “Comparative study of the lattice Boltzmann models for Allen-Cahn and Cahn-Hilliard equations,” *Phys. Rev. E* **94**, 033304 (2016).
- ³¹G.-S. Jiang and C.-W. Shu, “Efficient Implementation of Weighted ENO Schemes,” *Journal of Computational Physics* **126**, 202–228 (1996).

- ³²A. Harten, B. Engquist, S. Osher, and S. R. Chakravarthy, “Uniformly high order accurate essentially non-oscillatory schemes, III,” *Journal of Computational Physics* **71**, 231–303 (1987).
- ³³L. Laniewski-Wollk and J. Rokicki, “Adjoint Lattice Boltzmann for topology optimization on multi-GPU architecture,” *Computers and Mathematics with Applications* **71**, 833–848 (2016).
- ³⁴Z. Guo, K. Xu, and R. Wang, “Discrete unified gas kinetic scheme for all Knudsen number flows: Low-speed isothermal case,” *Phys. Rev. E* **88**, 033305 (2013).
- ³⁵Z. Guo, R. Wang, and K. Xu, “Discrete unified gas kinetic scheme for all Knudsen number flows. II. Thermal compressible case,” *Phys. Rev. E* **91**, 033313 (2015).
- ³⁶C. K. Aidun and J. R. Clausen, “Lattice-Boltzmann Method for Complex Flows,” *Annual Review of Fluid Mechanics* **42**, 439–472 (2010).
- ³⁷K. Xu and J.-C. Huang, “A unified gas-kinetic scheme for continuum and rarefied flows,” *Journal of Computational Physics* **229**, 7747–7764 (2010).
- ³⁸J. S. Rowlinson and B. Widom, *Molecular Theory of Capillarity* (1989).
- ³⁹C. Liu and J. Shen, “A phase field model for the mixture of two incompressible fluids and its approximation by a Fourier-spectral method,” *Physica D: Nonlinear Phenomena* **179**, 211–228 (2003).
- ⁴⁰D. Jacqmin, “An energy approach to the continuum surface tension method,” in *34th Aerospace sciences meeting and exhibit* (1996) p. 858.
- ⁴¹P. YUE, J. J. FENG, C. LIU, and J. SHEN, “A diffuse-interface method for simulating two-phase flows of complex fluids,” *Journal of Fluid Mechanics* **515**, 293–317 (2004).
- ⁴²C. Zhang, K. Yang, and Z. Guo, “A discrete unified gas-kinetic scheme for immiscible two-phase flows,” *International Journal of Heat and Mass Transfer* **126**, 1326–1336 (2018).
- ⁴³T. Chen, V. Chéron, Z. Guo, J. C. B. de Motta, T. Menard, and L.-P. Wang, “Simulation of immiscible two-phase flows based on a kinetic diffuse interface approach,” in *International Conference on Multiphase Flow* (2019).
- ⁴⁴H. Liang, B. C. Shi, Z. L. Guo, and Z. H. Chai, “Phase-field-based multiple-relaxation-time lattice Boltzmann model for incompressible multiphase flows,” *Phys. Rev. E* **89**, 053320 (2014).
- ⁴⁵M. Geier, A. Fakhari, and T. Lee, “Conservative phase-field lattice Boltzmann model for interface tracking equation,” *Phys. Rev. E* **91**, 063309 (2015).
- ⁴⁶X. He, S. Chen, and R. Zhang, “A Lattice Boltzmann Scheme for Incompressible Multiphase Flow and Its Application in Simulation of Rayleigh–Taylor Instability,” *Journal of Computational Physics* **152**, 642–663 (1999).

- ⁴⁷K. Yang and Z. Guo, “Lattice Boltzmann method for binary fluids based on mass-conserving quasi-incompressible phase-field theory,” *Phys. Rev. E* **93**, 043303 (2016).
- ⁴⁸P. L. Bhatnagar, E. P. Gross, and M. Krook, “A model for collision processes in gases,” *Phys. Rev.* **94**, 511–525 (1954).
- ⁴⁹S. Chapman and T. G. Cowling, *The Mathematical Theory of Non-Uniform Gases* (Cambridge University Press, 1970).
- ⁵⁰Y. Q. Zu and S. He, “Phase-field-based lattice Boltzmann model for incompressible binary fluid systems with density and viscosity contrasts,” *Phys. Rev. E* **87**, 043301 (2013).
- ⁵¹T. Chen, X. Wen, L.-P. Wang, Z. Guo, J. Wang, and S. Chen, “Simulation of three-dimensional compressible decaying isotropic turbulence using a redesigned discrete unified gas kinetic scheme,” *Physics of Fluids* **32**, 125104 (2020).
- ⁵²X.-D. Liu, S. Osher, and T. Chan, “Weighted Essentially Non-oscillatory Schemes,” *Journal of Computational Physics* **115**, 200–212 (1994).
- ⁵³D. Lycett-Brown and K. H. Luo, “Cascaded lattice boltzmann method with improved forcing scheme for large-density-ratio multiphase flow at high reynolds and weber numbers,” *Physical Review E* **94**, 053313 (2016).
- ⁵⁴A. Hamzehloo, P. Bartholomew, and S. Laizet, “Direct numerical simulations of incompressible rayleigh–taylor instabilities at low and medium atwood numbers,” *Physics of Fluids* **33**, 054114 (2021).
- ⁵⁵H. Ding, P. D. Spelt, and C. Shu, “Diffuse interface model for incompressible two-phase flows with large density ratios,” *Journal of Computational Physics* **226**, 2078–2095 (2007).
- ⁵⁶Q. Li, K. H. Luo, Y. J. Gao, and Y. L. He, “Additional interfacial force in lattice boltzmann models for incompressible multiphase flows,” *Phys. Rev. E* **85**, 026704 (2012).
- ⁵⁷F. Ren, B. Song, M. C. Sukop, and H. Hu, “Improved lattice Boltzmann modeling of binary flow based on the conservative Allen-Cahn equation,” *Phys. Rev. E* **94**, 023311 (2016).
- ⁵⁸C. Josserand and S. Zaleski, “Droplet splashing on a thin liquid film,” *Physics of fluids* **15**, 1650–1657 (2003).
- ⁵⁹T. Lee and C.-L. Lin, “A stable discretization of the lattice boltzmann equation for simulation of incompressible two-phase flows at high density ratio,” *Journal of Computational Physics* **206**, 16–47 (2005).
- ⁶⁰Y. Wang, C. Shu, H. Huang, and C. Teo, “Multiphase lattice boltzmann flux solver for incompressible multiphase flows with large density ratio,” *Journal of Computational Physics* **280**,

404–423 (2015).

⁶¹K.-L. Pan, P.-C. Chou, and Y.-J. Tseng, “Binary droplet collision at high weber number,” *Physical Review E* **80**, 036301 (2009).

⁶²X. He, R. Zhang, S. Chen, and G. D. Doolen, “On the three-dimensional Rayleigh–Taylor instability,” *Physics of Fluids* **11**, 1143–1152 (1999).

⁶³T. Chen, L.-P. Wang, J. Lai, and S. Chen, “Inverse design of mesoscopic models for compressible flow using the Chapman-Enskog analysis,” *Advances in Aerodynamics* **3** (2021).